Journal of Materials Chemistry C

Ferroic Phase Transitions and Magnetoelectric Coupling in Cobalt Doped BaTiO3

Journal:	*Journal of Materials Chemistry C*
Manuscript ID	TC-ART-06-2021-002961.R1
Article Type:	Paper
Date Submitted by the Author:	02-Aug-2021
Complete List of Authors:	Pradhan, Dhiren; University of Tennessee Knoxville College of Engineering, Materials Science and Engineering; Oak Ridge National Laboratory Center for Nanophase Materials Sciences, Mohanty, Hari; National Institute of Technology Rourkela, Department of Physics & Astronomy Kumari, Shalini; Pennsylvania State University University Park, Department of Physics Bhoi, Krishnamayee; National Institute of Technology Rourkela Department of Physics and Astronomy, Department of Physics and Astronomy Tang, Nan; The University of Tennessee Knoxville Department of Materials Science and Engineering Kant, Ravi; CSIR-National Physical Laboratory Rahaman, Md.; University of Rajshahi, Departmental of Materials Science and Engineering Pradhan, Dillip; NIT Rourkela, Department of Physics & Astronomy Kumar, Ashok; National Physical Laboratory (CSIR), Apex Level Standards & Industrial Metrology (ALSIM) Gilbert, Dustin; University of Tennessee Knoxville College of Engineering, Material Science and Engineering and Physics & Astronomy Rack, Philip; University of Tennessee,

Ferroic Phase Transitions and Magnetoelectric Coupling in Cobalt Doped $BaTiO_3$

Dhiren K. Pradhan[1,2*], Hari Sankar Mohanty[3], Shalini Kumari[4,5], Krishnamayee Bhoi [3], Nan Tang[1], Ravikant[6], M. M. Rahaman[7], Dillip K. Pradhan[3], Ashok Kumar[6], Dustin A. Gilbert[1,8], Philip D. Rack[1,2*]

[1]*Department of Materials Science & Engineering, University of Tennessee, Knoxville, Tennessee 37996, USA.*
[2]*Center for Nanophase Materials Sciences, Oak Ridge National Laboratory, Oak Ridge, Tennessee 37831, USA.*
[3]*Department of Physics & Astronomy, National Institute of Technology, Rourkela-769008, India.*
[4]*Department of Materials Science & Engineering, The Pennsylvania State University, University Park, Pennsylvania 16802, USA.*
[5] *Department of Physics, The Pennsylvania State University, University Park, Pennsylvania 16802, USA.*
[6]*National Physical Laboratory (CSIR), Dr. K. S. Krishnan Marg, New Delhi 110012, India.*
[7]*Departmental of Materials Science and Engineering, University of Rajshahi, Rajshahi 6205, Bangladesh.*
[8]*Department of Physics & Astronomy, University of Tennessee, Knoxville, Tennessee 37996, USA.*

Abstract

Magnetoelectric (ME) materials exhibit interesting physics with cross coupling between ferroelectric and magnetic order parameters and thus the strong potential to be utilized in memory, spintronics and other multifunctional electronic/magnetic devices. Doping of suitable transition metals in ferroelectrics can induce magnetism and ME coupling and modify the physical properties. Here, we report the structural, electronic, magnetic and ME coupling of 3.5, 5 and 7.5 mol% of cobalt doped $BaTiO_3$ (BTO) ceramics. X-ray diffraction and Raman spectroscopy indicate that the samples are single phase having tetragonal crystal structure with *P4mm* symmetry. The tetragonality ratio is found to decrease with increasing cobalt content. We observed a Fano-like asymmetric peak in the [$A_1(LO_1)$] Raman mode at ~ 173 cm^{-1} in all the cobalt doped BTO samples. The cobalt dopants are shown to be uniformly distributed throughout the surface of the samples. We observed a lowering of ferroelectric transition temperature and increasing the diffusive parameter with increasing cobalt concentration. The electrical properties of all the samples have been investigated in detail by impedance spectroscopy and ac conductivity studies before and after ferroelectric phase transitions. All the samples show hysteretic ferroelectric behavior with a clear saturation state that decreases with increasing cobalt content. The observed ferroelectricity in these samples is intrinsic in nature. 3.5 % cobalt doped BTO sample exhibits paramagnetic behavior whereas 5 and 7.5 % cobalt doped BTO samples show ferromagnetic orderings at below 43 K. The 7.5 % cobalt doped BTO samples shows significant ME coupling.

*Authors to whom correspondence to be addressed. Electronic mail: dhirenkumarp@gmail.com (Dhiren K. Pradhan), prack@utk.edu (Philip D. Rack).

Introduction

Magnetoelectric (ME) - Multiferroic (MF) materials are important multifunctional materials that exhibit spontaneous and switchable ferroelectric (FE) and (ferro/ferri/antiferro) magnetic orderings in a single phase. ME materials possess cross coupling among the magnetization and electrical polarization in which magnetization (polarization) can be switched/manipulated by applying suitable electric (magnetic field).[1-4] These materials have attracted significant attention because of their interesting physics and have potential to be utilized in ultralow power and high-density memory, energy storage and/or harvesting, spintronics, along with various multifunctional devices.[2-5] There are only a few single phase multiferroics that exhibit a simultaneous coexistence of the ferroelectric and magnetic orderings in one phase.[2, 6] The most studied and notable examples of single phase multiferroics includes Pb $(Fe_{0.5}Nb_{0.5})O_3$, $BiFeO_3$, $YMnO_3$, $BiMnO_3$, $TbMnO_3$, $GaFeO_3$, $YbMnO_3$, Pb $(Fe_{0.5}Ta_{0.5})O_3$, $LuMnO_3$ and $Pb(Fe_{0.67}W_{0.33})O_3$.[1, 2, 4, 7-9] Most of these materials exhibit a magnetic transition temperature (Currie temperature, T_{C-M}) well below room temperature and a ferroelectric critical temperature (T_{C-E}) well above room temperature, resulting in weak ME coupling.[10, 11] To observe robust ME coupling, dual phase MF composite architectures have been developed, which show much higher (several orders of magnitude) ME coupling than the single-phase systems.[4, 8, 11-14] These systems typically utilize strain to coupling intermediary between piezoelectric a magnetostrictive materials. However, for some specific applications and device configurations such as tunnel junctions, single phase systems are highly desired as electrical(magnetic) switching and control of magnetization(polarization) is much faster than the composite systems (where the coupling among the FE and magnetic orderings is mainly strain mediated).[2, 10, 15] Hence there is a large need to design new multiferroic materials exhibiting strong ME coupling at room temperature, which might lead to various energy efficient nano(micro)electronic, spintronics and memory devices.[3, 5] Generally, ferroelectric ordering in a material is favored which contain transition metals (TM) having empty *d* orbitals, whereas magnetic ordering is favored by partially filled *d* orbitals.[2, 6] Simultaneous FE and magnetic ordering along with ME coupling may be achievable by designing a TM perovskite with empty d orbitals, and doping it with ions that have partially filled orbitals.[16-19] However, ferromagnetism and ME coupling has been observed by doping of nonmagnetic palladium in $Pb(Zr_{0.2}Ti_{0.8})O_3$ (Pd:PZT) ceramics, which showed emergent ferromagnetic ordering with ME coupling.[15] There are some reports on the existence of ME coupling in TM doped Pb-based ferroelectric perovskites. [16-19] However, the Pb-based materials are not environmentally friendly and not compatible with the human body hence their applications in devices will be seriously limited in the near future.

BTO is one of the excellent lead-free, high-performance ferroelectric materials with a ferroelectric to paraelectric Tc ~ 398 K, which also possesses a large dielectric permittivity of ~ 3400 (at 1 kHz), low dielectric loss tangent ~ 0.017 (at 1kHz) along with large piezoelectric coefficients (d_{33} ~ 788 pC/N) at room temperature.[20-23] Recently, the effect of conduction band electrons on polarization switching and phonon dynamics of pure and doped $BaTiO_3$ have been studied theoretically. Their calculations suggest that conduction band electrons can lower the FE T_C and might even be utilized to induce a purely displacive type of transition[24] Ultrafast switching of the FE polarization via optical pulses in $BaTiO_3$ makes it suitable candidate for device applications.[25] Cobalt is a ferromagnetic metal with multiple oxidation states. Nakayama et. al reported theoretical investigations of the magnetic properties in TM (V, Sc, Cr, Fe, Mn, Co, Cu and Ni) doped $BaTiO_3$ systems.[26] Several theoretical and experimental investigations have been carried out that show magnetism in Fe, Mn, V and Cr doped $BaTiO_3$.[26-32] Cao et. al predicted the induction of magnetism in Co-doped $BaTiO_3$ via first principle calculations.[28] However, experimental investigations showing the existence of magnetism and ME coupling in Co-doped BTO are limited. For instance, sol gel prepared Co-doped BTO revealed some paramagnetism[33], however in one thin film study with a large doping range were all non-magnetic[34],where another study revealed a thickness dependent ferromagnetic properties with a magnetic Curie temperature > 380K[35]. Luo et al.[36] revealed ferromagnetism at room temperature in Co-doped $Ba_{0.5}Sr_{0.5}TiO_3$ thin film, with a T_{C-M}) of 570 K and a ferroelectric transition temperature of 200K. Here, we have systematically studied the structure, electronic, magnetic and ME properties of Co-doped BTO ($BaTi_{1-x}Co_xO_3$ (BTCO) with x = 0.035, 0.05 and 0.075) ceramics. We did not synthesize the higher concentrations of Co (> x=0.075), as higher percentage of Co doping might lead to the clustering of Co in the material which might lead to the formation of secondary phases (such as hexagonal phases) along with several extrinsic effects, which are not the intrinsic/true properties of the single-phase materials. These materials show room temperature ferroelectricity and low temperature magnetism. The ferroelectric T_{C-E} is found to decrease with increasing Co content. Interestingly, we also observed the existence of significant ME coupling below the magnetic T_{C-M}.

Experimental Details

Polycrystalline ceramic oxides of $BaTi_{1-x}Co_xO_3$ (BTCO) with x = 0.035, 0.05 and 0.075 were synthesized by the sol-gel auto combustion method using high purity (> 99.99%) analytical grade precursors of $Ba(NO_3)_2$ (Alfa Aesar), $Ti[O(CH(CH_3)_2]_4$ (Alfa Aesar), $Co(NO_3)_2$ (Merck),

$C_6H_8O_7$ (Vectec) and Glycine (Merck). $BaTi_{1-x}Co_xO_3$ samples with x = 0.035, 0.05 and 0.075 are abbreviated as BTCO3, BTCO5 and BTCO7, respectively. First, stoichiometric amount of Ti-isopropoxide and metal nitrates were dissolved in distilled water followed by the addition of a small amount of HNO_3 (nitric acid). In the synthesis procedure of BTCO samples the optimized ratio of fuel to oxidizer were maintained as C:N (citrate:nitrate) = 1.3:1 and G:N (Glycine:nitrate) = 1:1. Ammonium hydroxide was subsequently added to the solution to maintain a pH value of 7. Thereafter, we heated the clear solution on a hot plate to promote gelation and the gel was then dried at 180 °C to get a voluminous and spongy combustion residue. The final combustion residue was calcined in air atmosphere at an optimized temperature of ~ 850 °C for 6 h with a heating rate of ~ 5 °C/min. After the calcination, the powder was ground using an agate mortar and mixed with 3 wt % of polyvinyl alcohol (PVA) solution. The PVA mixed powder was shaped to cylindrical pellets having diameter of ~10 mm using a hydraulic press with a uniaxial pressure of 5 ton. The ceramic pellets were then sintered in a furnace in air atmosphere at optimized temperature of ~ 1200 °C for 6 h with a heating rate of 5 °C/min. The phase purity of the sintered pellets was measured with an X-ray diffractometer (Bruker D2 Phaser) having a CuK_α (λ=1.5405 Å) radiation source operating in the Bragg–Brentano (BB) geometry at 30 kV and 10 mA with a slow-scan speed of 0.5°/min in Bragg angles ranges from 20 – 80° having a step size of 0.02°. The Rietveld refinements of the X-ray diffraction (XRD) spectra were carried out using the FullProf Suite Software. Raman scattering studies were performed at RT using a Horiba Jobin Yvon T64000 system. The wavelength of 514.5 nm of the Ar ion laser was utilized as the excitation source. The existence of all elements and valence states the synthesized pellets were investigated via high-resolution X-ray photoelectron spectroscopy (XPS). Microstructural studies were performed using a Zeiss EVO field emission scanning electron microscope (SEM) using a Zeiss EVO SEM equipped with an energy dispersive x-ray spectrometer (EDS) system (Bruker) operated with an accelerating voltage of 15 - 30 kV. For the electrical and ferroelectric measurements, we polished the flat surface of the sintered ceramic pellets with very fine emery paper and made bottom and top electrodes by coating with highly pure silver paint. Then the silver coated pellets were heated at 100 °C for 1 h on a hot plate for better adhesion and conduction. The temperature dependent dielectric parameters, i.e., capacitance, loss tangent, impedance and phase angles were measured with fixed ac voltage of 500 mV in a large frequency range 100 Hz – 1 MHz using a high precision impedance analyzer (Hioki IM3570). Thermal control with precision was achieved with LINKAM heating stage in the temperature range of 300-600 K. Room

temperature ferroelectric hysteresis loops and positive-up negative-down (PUND) measurements of the samples were measured utilizing a Radiant RT 6000 HVS system at different frequencies. The electrical poling the samples was carried out using a high voltage DC Power supply (TREK:677A). The leakage current characteristics were measured through current-voltage (I-V) measurements with a lock in amplifier in the top-bottom configuration at room temperature. Magnetization measurements, including temperature and magnetic field dependence and ME coupling, were performed at 2 - 400 K on a Dynacool Physical Properties Measurement System (PPMS) from Quantum Design using the vibrating sample magnetometer (VSM) option.

Results and discussion

Structural Characterization:

The phase purity and crystal structure of BTCO3, BTCO5 and BTCO7 samples were investigated measuring the XRD at room temperature (Fig. 1(a)). The sharp and well-defined XRD peaks indicate the formation of crystalline perovskite compounds. The XRD patterns of BTCO samples are similar to the diffraction pattern of the pure $BaTiO_3$ sample. We did not observe any secondary phases in the XRD patterns within the resolution limit of the instrument, which suggests that the samples are single phase and phase pure. The crystal structure and the effect of cobalt doping on the lattice parameters and cell volume are further studied in detail by carrying out the Rietveld refinement using Fullprof package.[37] The Rietveld refinement was performed by considering *P4mm* space group with tetragonal crystal structure similar to the $BaTiO_3$.[38] We have used the pseudo-Voigt function for the peak refinement process. Various parameters such as scale factor, background, zero correction, lattice parameter, half width parameters, etc. have been determined during the refinement process. A good match between the experimental and simulated data is observed for all the compositions with the goodness of fit parameters (χ^2) = 2.36, 2.14, 2.54 for BTCO3, BTCO5 and BTCO7, respectively. The lattice parameters of BTCO3, BTCO5 and BTCO7 are found to be (a=b) = 3.9933 (4), 4.0015 (2), 4.0068 (2) and c= 4.0221 (5), 4.0268 (3), 4.0288(2), respectively. The unit cell volume is observed to be 64.1381, 64.4771 and 64.6802 $Å^3$ for BTCO3, BTCO5 and BTCO7, respectively. The increase in the lattice parameters and unit cell volume with an increase in the Co concentration are in agreement with literature.[39] The increase of unit cell volume and lattice parameters with an increase in cobalt content suggesting the development of localized tensile strain via Co doping. This might be due to the mismatch of ionic radii of the Co^{3+} / Co^{2+} ion

and Ti ion (with r_{ion} = 0.605Å) in the BTCO samples. The tetragonality ratio (c/a) is found to decrease with increasing cobalt concentration. The crystal structure of BTCO sample is shown in Fig. 1(b), where the Co^{+3} is assumed to substitute for Ti^{4+} which is likely compensated by an oxygen vacancy complex. Cao *et al*. theoretically predicted that the Co atoms prefer to occupy at the Ti site of $BaTiO_3$ by the formation energy. [28]

Raman Spectroscopy:

The Co-doped BTO Raman spectra contain a lot of rich spectral information. As described below there are three main observations that have been made from the analysis of the Raman data: 1) identification of the main peaks suggest the materials are single phase with tetragonal symmetry, in good agreement with our XRD; 2) there is an observed Fano resonance at 173 cm^{-1} which is attributed to the interaction of the discrete $A_1(LO_1)$ phonon and the broad central peak (CP), where the breadth of the CP is due to rapid polarization fluctuations in PNRs; and 3) the central peak narrowing with Co doping is suggestive of a slowing down of the precursor dynamics consistent with an increase in the size or number density of nanodomain states. The final observation is supported by the damping and phase shift observed in the lowest frequency mode ($E(TO_1)$).

Spectrum Overview and Phase Identification

Raman spectroscopy is one of the most sensitive tools to probe local heterogeneities due to compositional and structural disorder in ferroelectric/multiferroic materials. Therefore, the composition dependence of Raman spectra have been studied to realize the effect of Co-doping in BTO ceramics. The reduced intensity, $I^r(\omega)$ was computed from stokes components of observed Raman scattering intensity, $I(\omega)$, using the equation given below to avoid the influence of Bose-Einstein phonon population.[40-42]

$$I^r(\omega) = \frac{I(\omega)}{\omega[n(\omega)+1]} \quad \text{.....(1)}$$

where, $n(\omega) = \frac{1}{\exp\left(\frac{\hbar\omega}{k_B T}\right) - 1}$ is the Bose-Einstein population factor. k_B and $\hbar$ are Boltzmann and Dirac constants, respectively. To investigate the central peak (CP), which is generally related to the relaxation process of local polar clusters or polar nanoregions (PNRs), all reduced spectra were fitted in the frequency range 50-900 cm^{-1} by combining a Lorentzian central peak, damped harmonic oscillator (DHO) model, and a Fano function as follows:[40-42]

$$I^r(\omega) = \frac{2A_{CP}}{\pi}\frac{\Gamma_{CP}}{4\omega^2 + \Gamma_{CP}^2} + \sum_i \frac{A_i\Gamma_i\omega_i^2}{(\omega^2 - \omega_i^2)^2 + \omega^2\Gamma_i^2} + \frac{I_0(q+\varepsilon)^2}{(1+\varepsilon^2)} \quad \text{..... (2)}$$

Where, A_{CP} and Γ_{CP} denote the intensity and full width at half maximum (FWHM) of the CP, respectively. ω_i, Γ_i, and A_i denote the frequency, damping constant, and intensity of the i^{th} optical Raman active mode, respectively. I_0 is the intensity of the Fano resonance [A_1(LO$_1$) mode], q denotes the asymmetry parameter, which corresponds to the coupling strength between the continuum states and phonon, $\varepsilon = 2(\omega - \omega_{A1(LO1)})/\Gamma_{A1(LO1)}$ is the reduced energy, where $\Gamma_{A1(LO1)}$ is the FWHM of the Fano resonance. The fitted Raman spectra using Eq. (2) are shown in Fig. 2(a).

The Raman optic modes in the cubic phase with $\boldsymbol{Pm\bar{3}m}$ symmetry of $BaTiO_3$ transform as the $3T_{1u}+T_{2u}$ irreducible presentations. The F_{1u} modes are only infrared active and the F_{2u} mode is silent, and so there is no Raman activity in the paraelectric phase with perfect cubic symmetry. All the phonons become Raman-active in the tetragonal ferroelectric phase. In the tetragonal phase with *P4mm* symmetry, each of the T_{1u} mode generally splits into modes of A_1+E symmetry and the T_{2u} mode splits into modes of B_1+E symmetry. All the A_1 and E modes are both Raman and infrared (IR) active whereas the B_1 mode is only Raman active. Therefore, Raman active modes of the tetragonal crystal structure having *P*4*mm* crystal symmetry are represented by $3A_1+B_1+4E$. The long-range electrostatic forces normally induce the splitting of transverse and longitudinal phonons, which causes in split Raman active phonons described by $3[A_1(TO) + A_1(LO)] + B_1 + 4[E(TO) + E(LO)]$. The direct assignments of mode symmetries in polycrystalline ceramics are not possible from the Raman measurements. The detailed assignments of mode symmetries of $BaTiO_3$ reported elsewhere.[43-47]

The Raman spectra of Co-doped BTO ceramics measured at room temperature are displayed in Fig. 2(a). It is found that the Raman spectrum of the BTCO3 sample in the frequency range of 50~900 cm^{-1} consist of mainly E(TO$_1$) (~ 105 cm^{-1}), A_1(TO$_1$) (~161 cm^{-1}), A_1(LO$_1$) (~173 cm^{-1}), A_1(TO$_2$) (~247 cm^{-1}) E(TO$_2$)/E (LO$_1$) /B_1 (~298 cm^{-1}), E(LO$_2$) (~428 cm^{-1}), E(TO$_3$) (~497 cm^{-1}) A_1(TO$_3$) (~532 cm^{-1}), and E(LO$_3$) (~702 cm^{-1}), and A_1(LO$_2$) (~754 cm^{-1}) as shown in the upper part of Fig. 2(a). The broad peak near 327 cm^{-1} in Co-doped BTO may correspond to silent modes, which stem from higher order processes.[45] The dominant features observed for room temperature Co-doped BTO ceramics are: a symmetric peak near 161 cm^{-1} [A_1(TO$_1$], Fano-like asymmetric peak at around 173 cm^{-1} [A(LO$_1$)], a sharp peak at about 298 cm^{-1} [E(TO$_2$)/ E(LO$_1$))/B_1], asymmetric broad peak near 247 cm^{-1} [A_1(TO$_2$)], symmetric intense peaks near 497 cm^{-1} [E(TO$_3$)], and a symmetric broad intense peak at about 702 cm^{-1} [E(LO$_3$)], which

correspond to the tetragonal phase of the BTO.[43 48] The formation of the peaks near 515 cm^{-1} and 717 cm^{-1} correspond to the honon vibrations of the Ba-O bonds, whereas the observation of peaks near 173 cm^{-1} and 247 cm^{-1} correspond to the phonon vibrations of Ti-O bonds. We did not observe any sign of intense low frequency B_2 modes at around 60 cm^{-1} in the Raman spectra, which emerge in orthorhombic and rhombohedral phases of $BaTiO_3$ single crystals.[49] Besides phonon modes assigned to the tetragonal phase, an additional weak peak is observed around 600 cm^{-1} as shown in Fig. 2(a). In Fe-doped BTO, Dang *et al*. also found a peak around 610 cm^{-1}, which was attributed to incorporation of Fe^{3+} and Fe^{4+} ions having different ionic radii into the Ti^{4+} sites.[50] Thus, the Raman mode of Co-doped BTO near 600 cm^{-1} is likely due to the incorporation Co^{3+} ions with different ionic radii into the Ti^{4+} sites. Therefore, the BTCO samples in this study belongs to the tetragonal phase with *P4mm* symmetry. The tetragonal phase of BTCO samples is consistent with the Rietveld refinement of the XRD pattern.

Fano Resonance

It is interesting that the Raman spectra of BTCO samples are well fitted using the Fano function at ~173 cm^{-1} [$A_1(LO_1)$] as shown in Fig. 2(a). The phenomenon of a Fano resonance generally arises due to the interaction between continuum states and a discrete state exhibiting an asymmetry of the spectral line shape.[51] However, the physical origin of the Fano resonance at around 173 cm^{-1} in Co-doped BTO is unclear. In pure BTO single crystals, Rousseau and Porto[52] reported that the Fano resonance near 175 cm^{-1} is attributable to the interference effect arising due to the coupling between a single phonon state to a two acoustical phonon state via the anharmonic terms in the potential function. Pinczuk *et al*.[53] also reported that the interference near 175 cm^{-1} in pure BTO crystals may be due to the anharmonic coupling of the lowest frequency transverse optic (TO) phonon with the higher frequency TO phonon via acoustic phonons. The acoustic phonon mode is not observed in Co-doped BTO in this study, while the prominent Fano resonance is present. Therefore, the coupling between the acoustic phonons and the $A_1(LO_1)$ phonon is not ascribed to the origin of the Fano resonance in cobalt doped BTO samples. The Fano resonance at around 173 cm^{-1} of pure BTO was also attributed to the anharmonic coupling among the three $A_1(TO)$ phonons studied by Venkateswaran *et al*.[43] In Co-doped BTO, we failed to fit the Raman spectrum considering Fano resonance of the $A_1(TO_1)$ mode, while the spectrum was well fitted assuming Fano resonance at $A_1(LO_1)$ phonon, and this fact rules out the coupling among three $A_1(TO)$ phonons as the origin of Fano resonance in Co-doped BTO ceramics. In general the interference with a continuum of electronic states is characterized by a negative value of q.[54] However, the Fano resonance at around 173 cm^{-1} of Co-doped BTO samples in this study is well fitted with the positive value

about $q \sim 0.45 \pm 0.11$. Recently, Rahaman *et al*. reported the physical origin of a Fano resonance with a positive q value near 196 cm^{-1} in a Li-doped $KTa_{1-x}Nb_xO_3$ (x=0.27) single crystal. The Fano resonance was attributed to the coupling between the TO_2 phonon and the broad CP, which was attributed to polarization fluctuations in PNRs.[40-42, 55] The prominent CP of Co-doped BTO ceramics has been observed as shown in Fig. 2(a). The interference with the polarization fluctuations in PNR continua was also characterized by a positive value of q studied by Banerjee *et al*.[54]. So, the possible origin of the Fano resonance in Co-doped BTO ceramics is the coupling between a discrete $A_1(LO_1)$ phonon and the broad CP, due to rapid polarization fluctuations in PNRs.

Central Peak Behavior

In order to have a better understanding of the effects of Co doping on central peak (CP) in BTO, we have studied the CP behavior as a function of composition (Fig. 2 (b)). The CP expresses the general property of either a crystal or a ceramic undergoing the order-disorder phase transformation, while soft phonon modes is a common property of the displacive phase transition of ferroelectric materials. Pure BTO was originally considered to belong to the class of displacive-type ferroelectric materials where the soft mode plays an important role.[56] Recently, the soft mode behavior of BTO has also been studied as a function of photoexcited electron density by density functional theory (DFT).[24] Brillouin scattering of the CP, was used to study the order-disorder nature of ferroelectric phase transition of a BTO single crystal, which is caused by polarization fluctuations of PNRs.[55] It is well accepted that the order-disorder and displacive phase transition coexist in BTO.[57] By Raman scattering, the coexistence of the displacive and order-disorder phase transition was also found in ferroelectric $KNbO_3$ by observing soft mode and the CP, respectively.[58] It is difficult to comment on the soft-mode nature because of the lack of temperature dependent Raman scattering results. So, the presence of the broad CP can be an indication of the order-disorder nature of ferroelectric phase transition of Co-doped BTO ceramics. It is well established that the fluctuating PNRs start to appear in a paraelectric cubic phase at the so called Burns temperature (T_B),[59] whereas a dynamic to static transition of these PNRs begins at an intermediate temperature (T^*). [41, 42] However, these static PNRs becomes randomly oriented nano-domain states due to the freezing out of polarization in the ferroelectric phase.[40] It is important to note that the full width at half maximum (FWHM) of the CP, which is inversely proportional to the relaxation time of precursor dynamics,[60] decreases with increasing cobalt dopants in BTO as shown in upper panel of Fig. 2(c). The relaxation time of the precursor dynamics in BTO was previously

estimated by Brillouin scattering.[55] Furthermore, by Raman scattering, the slowing down of precursor dynamics was also examined by narrowing the CP upon cooling.[41,61] It is apparent from Fig. 2(b) that the CP becomes narrower by Co-doping to BTO, implying a slowing down of the precursor dynamics. This result suggests that size and/or the number density of randomly oriented nano-domain states may increase with increasing Co dopant in BTO, which enhances the relaxation process. It is also expected that the enhanced size and/or number density of randomly oriented nano-domains may affect the observed lowest possible Raman active mode of Co-doped BTO ceramics. Thus, we studied the Raman mode at around 105 cm^{-1} of Co-doped BTO as a function of composition. The frequency shift and damping of the $E(TO_1)$ mode at ~105 cm^{-1} of Co-doped BTO is displayed in the lower panel of Fig. 2(c). It is worth noting that the frequency of the mode near 105 cm^{-1} slightly decreases with increasing of cobalt concentrations. The optical phonon mode near 105 cm^{-1} significantly scatters by the randomly oriented nano-domain states, thereby the damping increases, while frequency decreases (lower panel of Fig. 2 (c)). The results indicate that the variations of shape and size of the mode around 105 cm^{-1} is affected by the size and/or number density of randomly oriented nano-domains and their compositions.

XPS Studies:

Figure 3 shows high resolution x-ray photoelectron spectroscopy (XPS) spectra of a BTCO7 sample as representative of the BTCO samples. The core level high resolution XPS spectra of Ba 3*d*, Ti 2*p*, Co 2*p,* and O 1*s* were observed. As there is a direct overlap between Ba 3*d* and Co 2*p* peaks, thus to further confirm the presence of cobalt, we also examined the Co 3*s* peak (as the Co LMM Auger peak is below the detection limit). Charge correction has been done using the C 1*s* peak shifted to 284.8 eV. As has been discussed previously, the photoelectron peaks of Ba $3d_{3/2}$ and Ba $3d_{1/2}$ peaks typically have contributions from the perovskite phase (α) and a relaxed perovskite (β) due to oxygen vacancy and residual defects[62, 63]. As shown in figure in figure 3, the peaks of the α Ba $3d_{3/2}$ (778.41 eV) and Ba $3d_{1/2}$ (793.43 eV) are larger than the slightly high-energy shifted β Ba $3d_{3/2}$ (780.33 eV) and Ba $3d_{1/2}$ (795.35 eV).

The Co $2p_{3/2}$ (780.90 eV) and Co $2p_{1/2}$ (796.31 eV) peaks overlap with the Ba 3d peaks and have similar spin-orbit splitting (Δ=15.41 eV) and (Δ=15.02 eV), respectively. Because of the Ba/Co ratio (~ 13) and Ba has a higher sensitivity factor than Co, we are not able to discern the specific Co valence state. Previous reports have conflicting results where x-ray absorption near-edge spectroscopy has suggested +2 in Co-doped BSTO[36] and +3 in Co -doped BTO[35]. From figure 3, the Co $2p_{1/2}$/Co $2p_{3/2}$ and Co 3*s* peaks were fitted with a single

Gaussian-Lorentzian peak Petitto et al.[64] , showed that the spin orbit split *2p* peaks of the Co^{+2} oxidation state (CoO) have satellite peaks at ~ +6 eV binding energy with peak intensities with approximately half of the $2p_{1/2}$ and $2p_{3/2}$ peaks. For the +3-oxidation state (Co_3O_4), however, the satellite peaks are greatly reduced. The low Co concentration and overlap with the Ba 3d peaks however make distinguishing the oxidation state not possible. Due to the doping of Co (+2 or +3) at Ti (+4) sites, there should be formation of oxygen vacancies. The peak observed at higher binding energy (~ 534.3 eV) corresponds to the presence of oxygen vacancies (Fig 3 (d)). Similar types of observations have been reported attributing the higher binding energy peak to the presence of oxygen vacancies.[65, 66] Finally the Ti $2p_{3/2}$ (457.81 eV), Ti $2p_{1/2}$ (463.56 eV), O 1*s* (531.58 eV), Ba $4d_{3/2}$ (90.54eV), Ba $4d_{1/2}$ (92.68 eV), and Co 3*s* (102.94 eV) were all observed (see survey spectrum in Supplementary material S1).[67, 68]

Scanning Electron Microscopy Studies:

The surface morphology and elemental mapping of the BTCO3, BTCO5 and BTCO7 samples were investigated by SEM imaging. The micrographs of BTCO7 are shown in Fig. 4(a) and are representative of all the samples. The microstructure is found to be globally dense having distinct grains and grain boundaries without any microcrack, but some scattered pores are observed. The polycrystalline behavior is observed in the micrograph having grains of different tetrahedral shapes and sizes, with edge lengths between $\approx 1 - 3$ μm. The inhomogeneous distributions of grains are found all over the surface of the sample. The micrographs of BTCO3 and BTCO5 samples are presented in Supplementary material S2 and S3 respectively. The elemental mapping on the BTCO7 sintered pellet was carried out to further confirm the presence of all the elements (Ba, Ti, Co and O) and to confirm a uniform distribution throughout the surface of the samples especially for Co as clustering of Co might lead to extrinsic magnetic properties (Fig. 4(a)). It is also possible that some of Co might segregate to the surfaces for higher doping concentrations. The color images having area ~ 25× 25 μm^2 demonstrate the quantitative analyses of all the elements present in the sample and we observed that Ba, Ti, Co and O are uniformly distributed on the surface of the samples within the resolution limit. The elemental mapping images of BTCO3 and BTCO5 samples are shown in Supplementary material S2 and S3 respectively. The distribution of all the elements even on a single grain have also been checked in BTCO7 sample and found that they are distributed homogeneously (Fig. 4(b)). We also captured the EDS spectra of all the elements in BTCO7 sample and observed distinct peaks from all the elements even though Co has a low concentration and overlaps with some Ba peaks (Supplementary material S4).

Dielectric Properties:

Phase transitions are intrinsically connected to the underpinning physics that driving the system. To investigate the behavior of the ferroelectric phase transition and to probe the transition temperature, we carried out temperature dependent relative dielectric permittivity (ε_r) and dielectric loss (tan δ) measurements of BTCO3, BTCO5 and BTCO7 samples at selected frequencies (Fig. 5 (a), (c), (e)). The dielectric permittivity decreases with increasing frequency for all the compositions, suggesting the polar dielectric nature. For all the compositions, the dielectric permittivity increases gradually with increasing temperature, attains a maximum value and then decreases irrespective of the frequencies. The temperature at which the dielectric permittivity is a maximum is the ferroelectric Curie temperature (T_{C-E}), where the system undergoes a phase transition from the lower symmetric ferroelectric to higher symmetric paraelectric phase. It has been observed that the T_{C-E} is the same for all the frequencies for a particular composition. Fig. 5 (a), (c), (e) also shows the variation of dielectric loss tangent as a function of temperature at selected frequencies (right side of Y- axis). The temperature dependent dielectric loss curves for all the samples also shows a peak around the T_{C-E}, which further confirms the ferroelectric-paraelectric phase transition. For all the BTCO samples, dielectric permittivity and loss tangent show similar temperature dependence and frequency, except the variation of phase transition temperature and maximum value of dielectric permittivity. However, another peak is found around 135^0C in the temperature dependent tan δ for BTCO3 samples. This second anomaly observed in dielectric loss plot might be associated with relaxation process of the high temperature thermally activated mobile charge carriers and/or space charge relaxation in paraelectric phase. Similar type of behavior has been observed in $Ka_{0.5}Na_{0.5}NbO_3$ based ferroelectrics[69] and Bi doped $SrTiO_3$ [70]. Pure $BaTiO_3$ exhibits a T_{C-E} ~ 125ºC. The T_{C-E} values of BTCO3, BTCO5 and BTCO7 samples are found to be 110, 100 and 95 ºC, respectively, where the maximum value of dielectric permittivity is 2950, 3265, 3587, respectively at the frequency of 10 kHz. Compared to the pure BTO the T_{C-E} is shifted towards lower temperature with increasing Co concentration. The lowering of T_{C-E} can be explained by the changes of the unit cell because of the doping of Co^{3+} ion having ionic radius ~ 0.68 or 0.75 Å (in low spin or high spin configuration, respectively), or Co^{2+} having ionic radius of ~ 0.79 or 0.885 Å (in low spin or high spin configuration, respectively) which is larger than that of Ti^{4+} (0.605 Å).[71] The mismatch of ionic radii causes a lattice distortion along with the modification of BO_6 octahedra hence changes the transition temperature and polarization behavior. The decrease of transition temperature with the substitution of larger cations was observed in various perovskites and related structures.[15, 72, 73]

To investigate the nature of the phase transition behavior, the temperature dependent dielectric behavior has been analyzed using modified Curie-Weiss law. Above the phase transition temperature i.e. in the paraelectric region; the temperature dependent dielectric permittivity for a normal ferroelectric material obeys Curie-Weiss law given by[74, 75]

$$\varepsilon_r = \frac{C}{T - T_0} \quad \text{..... (3)}$$

where C = Curie constant, T_0 is Curie temperature ($T_{C\text{-}E}$ ($T_{C\text{-}M}$) when applied to a ferroelectric (ferromagnet)) and T is the absolute temperature. However, for a disorder/relaxor ferroelectric material, the temperature dependent dielectric behavior can be modelled using modified Curie-Weiss law which is expressed by the equation [74, 76]

$$\frac{1}{\varepsilon_r} - \frac{1}{\varepsilon_m} = \frac{(T - T_C)^\gamma}{C}$$

……(4)

where $C = 2\varepsilon_m \delta^\gamma$ is modified Curie-Weiss constant. In equation (4) ε_m represent the maximum value of dielectric constant at $T_{C\text{-}E}$, γ is the degree of diffuseness/degree of relaxation and δ is the diffuseness parameter. The value of γ lies in the range of 1 to 2, if γ = 1 for a material, it exhibits normal ferroelectric behavior whereas for γ = 2, the material shows disorder/relaxor type behavior. To elucidate the nature of the phase transition behavior the temperature dependent dielectric data have been fitted using equation (4). The value of γ can be calculated from the slope of linear fit and intercept value gives the value of δ which can be calculated using the relation

$$\delta = \left(\frac{e^{-\text{int}ercept}}{2\varepsilon_m} \right)^{1/\gamma} \quad \text{..... (5)}$$

The modified Curie-Weiss law fit for BTCO3, BTCO5 and BTCO7 samples are shown in Fig.5 (b), (d) and (f) respectively. The value of γ for BTCO3 BTCO5 and BTCO7 is found to be 1.3, 1.15 and 1.1 respectively. As the value of γ is close to 1 for all the samples, suggesting normal ferroelectric behavior of the $BaTi_{1-x}Co_xO_3$ ceramics. The value of diffusive parameter δ for $BaTi_{1-x}Co_xO_3$, x = 0.035, 0.05, 0.075 is calculated to be 25.9, 27.2, and 28.7, respectively. The diffusivity parameter value increases with increasing Co concentration because of the pinning of ferroelectric domains with the lower resistive Co doping.

Impedance Spectroscopic Studies:

To distinguish the bulk and grain boundary contributions of the impedance we have performed impedance spectroscopy studies. Fig. 6 (a, b, c) show the Nyquist plot (- Z″ vs. Z′) at different temperatures of BTCO3, BTCO5 and BTCO7 samples respectively. The impedance spectra

are demonstrated by the presence of semi-circular arcs whose pattern changes with temperature and composition. For all the compositions, a single semi-circular arc is observed at all the investigated temperature range (except at very high temperatures). The presence of single semi-circular arc corresponds to the bulk properties of the material. To extract more information from this plot, we have fitted the experimental data using ZsimpWin 3.21 software. (R_bC_bQ) equivalent circuit is used to fit the experimental data for all compositions where (R_bC_bQ) represent the parallel combination of bulk resistance (R_b), bulk capacitance (C_b) and constant phase (Q). The justification of constant phase and the proposed equivalent circuit is mentioned elsewhere.[77] The proposed equivalent circuit is able to fit the experimental data for BTCO3, BTCO5 and BTCO7 samples and suggests the main contribution is from bulk response of the material. However, for very high temperature i.e. above 270 ^oC the (R_bC_bQ)($R_{gb}C_{gb}$) equivalent circuit is used for BTCO samples. Here, (R_bC_bQ)($R_{gb}C_{gb}$) represents series combination of (R_bC_bQ) and ($R_{gb}C_{gb}$) whereas ($R_{gb}C_{gb}$) is the parallel combination of grain boundary resistance and grain boundary capacitance. A good fit is observed with the proposed model at high temperature. It has been observed that grain/bulk resistance (obtained after fitting process) decrease with the increasing temperature, indicating the negative temperature coefficient of resistance (NTCR) behavior. The bulk conductivity has been plotted with the inverse of temperature and obey the Arrhenius relation given by $\sigma_{dc} = \sigma_p \exp(-E_a / k_B T)$, where σ_p is the pre-exponential factor, E_a is the activation energy and k_B is the Boltzmann constant. Two different slopes are observed below and above the $T_{C\text{-}E}$, thus there are two different relaxation processes associated with below and above the phase transition temperature. The activation energies are found to be ~ 0.20, 0.19, and 0.13 eV for BTCO3, BTCO5 and BTCO7 samples below the phase transition temperature, and 1.10, 0.8, 0.8 eV for BTCO3, BTCO5 and BTCO7 samples above the phase transition temperature, respectively.

Frequency dependent ac conductivity study:

To complement the impedance spectroscopy data, frequency dependent conductivity at different temperatures for BTCO3, BTCO5 and BTCO7 samples are shown in Fig. 7 (a, b, c) respectively. The ac conductivity was calculated using the relation $\sigma_{ac} = \omega \varepsilon_0 \varepsilon_r \tan\delta$, where ε_0 is the permittivity in free space, ε_r is the relative dielectric permittivity, ω is the angular frequency and $\tan\delta$ is the dielectric loss tangent[78]. It has been observed that the ac conductivity increases with increasing cobalt concentrations throughout the frequency range investigated. Similar observations have been reported in Fe doped BTO ceramics.[79] The ac conductivity is

characterized by the appearance of a frequency independent plateau in the low frequency region and frequency dispersion at high frequency. The frequency independent plateau corresponds to the dc conductivity of the materials. Similar type of behavior is also observed for other compositions. Such frequency dependence of the ac conductivity spectra can be explained by Johnscher's power law given by [78] $\sigma_{ac} = \sigma_{dc} + A\omega^n$ …… (6).

In this expression, σ_{dc} is the dc conductivity, A is the pre-exponential factor and n is the power law exponent. The parameter A is temperature dependent and the value of n lies between 0 and 1. We have fitted the experimental data using Johnscher's power law (except at very low frequency region) and observed a good fit between the experimental and simulated data as shown in the Fig.7. The temperature dependent dc conductivity (obtained from the fitting) is found to obey the Arrhenius relation given by $\sigma_{dc} = \sigma_p \exp(-E_a / k_B T)$, where σ_p is the pre-exponential factor, E_a is the activation energy for different slopes and k_B is the Boltzmann constant.

For all the compositions, the variation of dc conductivity with inverse of temperature (shown in the inset of figure 7), shows two different slopes below and above the ferroelectric phase transition temperature. The activation energy can be calculated from the slope of the linear fit using the Arrhenius relation. The different activation energy both below and above the phase transition temperature corresponds to different domain configurations and differences in the conduction mechanism.[80] When the phase transition occurs in the ferroelectric system, the phase transition is associated with the relaxation process of domain wall motion, domain orientations and dipolar behavior of the ferroelectric system.[80] In the ferroelectric region and similar to the impedance spectroscopy data, the lower value of the activation energy (0.35, 0.28, 0.12 eV for BTCO3, BTCO5 and BTCO7, respectively) suggest the high mobility domain wall and associated with the relaxation mechanism of small polarons, created by electron and/or hole-phonon interactions. The higher value of the activation energy above the phase transition temperature, which is also consistent with the impedance spectroscopy data (1.26, 1.10, 0.66 eV for BTCO3, BTCO5 and BTCO7, respectively) corresponds to doubly ionized oxygen vacancies, which is generally observed in dielectric oxides such as $SrTiO_3$, $KNbO_3$, etc.[81-83]

Ferroelectric and Leakage Current Studies:

The presence of ferroelectricity in the BTCO3, BTCO5 and BTCO7 samples were confirmed by measuring the electric field (E) dependence of polarization (P) loops of unpoled and poled samples at room temperature (Fig. 8 (a)). The ceramic samples were poled by applying dc-

electric field of ~ 10 kV/cm for 4 hours. The unpoled and poled samples of all the compositions exhibit well saturated ferroelectric hysteresis behavior confirming the existence of ferroelectricity in these samples. We observed a slight increase in saturation polarization by electrical poling of the samples as the applied electric fields align the randomly oriented ferroelectric domains in the direction of electric field. The electrical poling also traps the mobile free carriers at oxygen vacancies and stabilize the oxygen octahedra having less local inhomogeneities. It might also be possible that Co^{3+} /Co^{2+} cations act as defect centers that reduce the de-trapping of free carriers after poling the samples. The saturation polarization (Ps) of BTCO3, BTCO5 and BTCO7 samples are found to be ~ 27.6, 24.9, 21.7 μC/cm^2 respectively. The decrease of saturation polarization with increasing cobalt concentration is likely due to the pinning of ferroelectric domains by the magnetic material. We did not observe any systematic variation of coercive field (Ec) with increasing Co concentration.

Many non-ferroelectric materials show hysteretic behavior arising from charge injection and other extrinsic effects. To further confirm the observed ferroelectric behavior in the BTCO samples are intrinsic in nature, we carried out positive up negative down (PUND) measurements on BTCO5 samples (Fig 8 (b)). The upper panel shows the time profile of applied electric field. As shown in Fig 8 (b) (lower panel), we observed the net switchable polarization (dP) of ~ 2.5 μC/cm^2 and net switchable remanent polarization (dP_r) of ~ 4.3 μC/cm^2 .

Here, the net switchable polarization (dP) is defined as: $dP = P^* - P^\wedge$,

Here, P^* is (switchable + non-switchable) polarization, $P^\wedge$ is non-switchable polarization.

The net remanent switchable polarization $dP_r = P^*_r - P^\wedge_r$,

Here, P^*_r is (switchable + non-switchable) remnant polarization, $P^\wedge_r$ = non-switchable remnant polarization.

Hence, the PUND results demonstrate that the ferroelectric hysteresis behavior observed in our case are real and intrinsic in nature.

The leakage current behavior of BTCO3, BTCO5 and BTCO7 samples were investigated by measuring the current density (*J*) as function of dc electric field (*E*) of unpoled and electrically poled samples as shown in Fig 8 (c). The *J* - *E* plots show that the poled and unpoled samples for all the cobalt doping concentrations exhibit low leakage current and show symmetric behavior under the application of negative and positive electric fields. At near zero electric field, BTCO3 exhibits a current density of ~ 2.79 ×10^{-9} A/cm^2. With an increase in electric field, the current density increases rapidly to ± 7 kV/cm and then almost saturates with further increase of electric field in both positive and negative directions. The leakage current is found

to increase with increasing cobalt content in BTO; the cobalt doping pins the ferroelectric domain hence increases the conductivity and oxygen vacancies are also likely coupled to the Co^{3+}/Co^{2+} ion substituting in the Ti^{4+} site. The leakage current found in BTCO samples are much lower than other single phase multiferroics such as $BiFeO_3$.

The effect of electrical poling on the leakage current is also investigated for BTCO3 samples by performing the J-E measurements of unpoled and poled samples and shown in inset of Fig. 8 (c). The leakage current of poled sample is found to be slightly lower than the unpoled sample. Electrical poling orients the randomly oriented domains, which reduces the domain wall pinning and compensates the defect density, which in turn enhances the resistivity. It is also possible that the deficiency of charge carriers at cobalt defect centers along with the associated oxygen vacancies might be overcome by the free charge carriers via electrical poling. These free charge carriers gain sufficient energy from external applied electric field to move between centers and compensate defects, which makes the octahedra more stable and enhances the net dipole moments and lowers the leakage current.

Magnetic Properties:

The magnetic properties in BTCO samples have been investigated by measuring the magnetization (*M*) of a small piece of the sintered sample as a function of in-plane magnetic field (*H*) and temperature (*T*). The M(T) measurements were performed by measuring the magnetization while the sample was cooled from 300 K to 2 K in magnetic fields of 100 Oe and 1000 Oe. The M(H) measurements were performed at select temperatures in this range, spanning magnetic fields up to 9 T. The *M*(*T*) and M(H) curves of BTCO3 and BTCO5 samples are shown in Fig. 9. The *M*(*T*) curve for the BTCO3 sample shows a continuously increasing and trend, always with positive magnetization, and diverging approaching 0 K, suggesting paramagnetic behavior, Fig. 9(a). Plotting the inverse susceptibility ($1/\chi$), shown in the inset, confirms a linear trend in BTCO3, consistent with paramagnetic behavior. The *M*(*H*) plots for the BTCO3 sample, Fig. 9(b)show a paramagnetic field response, with a positive, linear field response for T > 50 K, resolving to a sigmoidal shape approaching low temperatures, but always remaining closed. This suggests Pauli paramagnetic behavior likely from Co ions, which are effectively isolated. At the lowest temperatures, the magnetization is ≈1 μ_B/Co, indicating that many of the Co ions are in the intermediate or high-spin configuration, comparing this to the BTCO5, the *M*(*T*) curve shows a clear bump at ≈ 42 K atop a similar divergent curve. The $1/\chi$ plot (Fig. 9c inset) shows linear behavior at higher temperatures, but becomes non-linear below ≈80 K, indicating a divergence from simple paramagnetic behavior.

The $M(H)$ plots continue to show a linear field response for T > 50 K, however measurements at 10 K now show an open hysteresis loop with remanent magnetization (M_r) of ≈ 0.019 emu/g and coercive field (H_c) of ≈0.98 kOe, indicating a ferromagnetic transition. The commensurate opening of the hysteresis loop and bump in the $M(T)$ data suggests a correlation – that the bump identifies the Curie temperature, however it is unusual for the magnetization to subsequently decrease, which is more typical of an antiferromagnetic transition. Antiferromagnetic ordering may simultaneously exist within this material due to oxygen mediated superexchange interactions.

Measurements of the BTCO7 sample, shown in Fig. 10, have a $M(T)$ curve similar to BTCO5, showing a bump at 43 K. The $M(H)$ curves again show a linear field response at T >50 K and an open hysteresis loop at all temperatures T<50 K. The inverse susceptibility measurements, Fig. 10a insert, shows non-linearity below ≈200 K, indicating a divergence from simple paramagnetic behavior throughout most of the measurement, possibly being antiferromagnetic or frustrated magnetization. Interestingly, for 6 K < T < 50 K, the magnetic coercivity increases with decreasing temperature, as would be expected with the suppression of thermally activated reversal mechanisms. However, for T< 6 K, H_C rapidly decreases, and virtually disappears at T=2 K. Since the magnetic transition temperature is consistent between the 5% and 7.5% samples, this suggests the observed transition is not superparamagnetism – larger clusters would be expected in the 7.5% sample, increasing the blocking temperature. Furthermore, the constant increase in magnetization with decreasing temperature, after the 43 K bump, suggests this is not emergent antiferromagnetism. One possible explanation for the decreasing coercivity is that, at the lowest temperatures, the ME coupling increases, resulting in an effective anisotropy, which is randomly oriented due to the polycrystalline structure.

At low temperature (< 30 K), the magnetization is found to be negative for both BTCO5 and BTCO7 samples when the external applied dc magnetic field is 100 Oe. The observation of negative remanent magnetization at low temperature and low applied magnetic field in BTCO5 and BTCO7 samples might be due to the phase coexistence of ferromagnetic and superparamagnetic phases. This unusual behavior might also be linked to the dipolar interaction between the ferromagnetic Co ions and superparamagnetic Co ions. Similar type of observations (i,e negative remanent magnetization at lower field at lower temperature) have been observed in a randomly distributed cobalt nanoparticle system[84] and ferromagnetic $La_{0.7}Sr_{0.3}MnO_3$ thin films.[85, 86] Negative magnetization also occurs at low temperatures due to trapping of free charge carriers, vacancies across the grains and grain boundaries.

As described above, the experimental literature on the magnetism in BTCO is inconsistent. Density functional theory (DFT) calculations of various geometries [34] suggest that the low energy state of an isolated Co^{4+} substitution into the Ti^{4+} (Co^{4+}_{Ti4+}) octahedra is the low spin state with a 1 Bohr magneton (μB) moment. For two neighboring Co^{4+}_{Ti4+} substitutional atoms the intermediate spin state is the lowest energy and the basal and apical geometries both have a total magnetization ~ 6 μB. A pair of negatively charged Co'_{Ti} centers (where cobalt is in the +3 valence state) can be stabilized by an oxygen vacancy ($V_O^{\bullet\bullet}$), and the lowest energy state of this $(2Co'_{Ti} - V_O^{\bullet\bullet})^{\bullet}$ complex and for both the basal and apical configurations is the high spin antiferromagnetic configuration with μ_{Co}=+-2.96 μ_B. Finally, a Co''_{Ti} can be stabilized with neighboring $V_O^{\bullet\bullet}$ [$(Co''_{Ti} - V_O^{\bullet\bullet})^{\times}$] (where cobalt is in the +2 valence state) and at higher Co concentrations $(Co''_{Ti} - V_O^{\bullet\bullet})^{\times}$ pairs are possible with various orientations. The single $(Co''_{Ti} - V_O^{\bullet\bullet})^{\times}$ has a low spin state as the lowest energy state, which has a total moment of 3 μB. Finally, several orientations for the $(Co''_{Ti} - V_O^{\bullet\bullet})^{\times}$ pairs are possible, and the lowest energy state (2 Co''_{Ti} and 1 $V_O^{\bullet\bullet}$ are all basal and 1 perpendicular apical $V_O^{\bullet\bullet}$) state is the antiferromagnetically coupled high spin state with a μ_{Co}= +2.61 μ_B and μ_{Co}= - 2.52 μ_B, where the slight difference is due to magnetization on the neighboring oxygen. Based on our maximum measured magnetization, we estimated μ_{Co} for the 3.5, 5 and 7.5% BTCO are ~ 1.1, 0.7 and 0.5 μ_B, respectively. Our XPS results of the BTCO7 sample could not rule out the Co^{3+} state, which the DFT calculations suggest should be non-magnetic. We posit that the $(2Co'_{Ti} - V_O^{\bullet\bullet})^{\bullet}$ could be more extended than simple nearest neighbors, which could relax the antiferromagnetic coupling; the lower concentration BTCO samples will logically have more extended defects as the Co-Co average distance increases. Additionally, at lower Co concentrations (though beyond our XPS sensitivity), the cobalt could be in the 4+ state (fewer $V_O^{\bullet\bullet}$), which would increase the μ_{Co} and is consistent with the lower resistivity. It should also be noted that the energy difference between many of the calculated magnetic states were only several to tens of meV different, thus slight changes in the defect complexes could induce magnetism.

Magnetoelectric Coupling:

Existence of magnetoelectric coupling was demonstrated by measuring the magnetization of the BTCO7 sample at 20 K with an *in situ* electric field of 3 kV cm^{-1} applied parallel to the magnetic field and measurement axes, e.g. a longitudinal configuration.

Measurements of the as prepared (pressed, sintered) sample, Fig. 11, showed a two-step reversal, with a major loop coercivity of 60 mT and a remanence (M_R=M(H=0)/M_S) of ≈ 0.39. The two steps are distributed such that the low-coercivity feature accounts for 68% of the magnetic signal; the harder magnetic phase accounts for 32% and has an apparent saturation field of 650 mT. Measurements on the as-prepared sample shown in Fig. 10(b) have a similar saturation field and loop shape as the harder phase, suggesting this phase is representative of the Co doped BTO, while the soft phase may be due to sample aging. Applying the *in situ* electric field, the hysteresis loop shows an enhanced major loop coercivity and a redistribution of the magnetic weight between the steps in the reversal towards the higher coercivity component. Specifically, the major loop coercivity increased to 90 mT and the low-coercivity feature now accounts for 58% of the magnetic weight. Notably, the remanence remains virtually unchanged. Subsequently reversing or otherwise reducing the strength of the electric field did not significantly affect the magnetization behavior.

Changes to the magnetic reversal behavior are consistent with magneto-electric coupling. The as-prepared sample is expected to possess tetragonally distorted ferroelectric domains with random orientations due to the powdered microstructure. Applying an electric field augments the distribution, causing domains with the ferroelectric ordering and tetragonal distortion parallel to the electric field to grow. Alternatively, domains may re-orient to align their ferroelectric polarization axis with the electric field. The magnetization measurements showed that this caused the high coercivity phase to grow. Following the Stoner–Wohlfarth model, measurements performed along the magnetic easy axis show the highest coercivity due to the necessity to rotate the moment through the hard axis. The Stoner–Wohlfarth model also suggests that measurements along the magnetic hard axis have a small coercivity and can appear nearly reversible. The observed increase in the high coercivity phase and decrease in the very small coercivity soft phase suggests that the tetragonal distortion corresponds to the magnetic easy axis. The insensitivity to further electric field treatments likely indicates that the magnitude of the electric field is insufficient to cause further domain growth. Complementary, the polarity of the electric field does not change the orientation of the tetragonal distortion and so would not affect the magnetic response, as observed in the hysteresis loops. The significant change in the coercive field and remanent magnetization with an *in situ* electric field indicates the strong coupling between the ferroelectric and magnetic orderings.

When any electric field is applied to a magnetoelectric (ME) system, the ferroelectric domains align in the direction of electric field. As the ferroelectric and magnetic domains are coupled, hence the orientation of magnetic domains will be changed with the

application of electric field which will give rise to the modification of the magnetic order parameters. Hence, existence of ME coupling can be confirmed from these measurements. A significant change in magnetic orderings by applying an electric field less than the coercive field indicates the existence of ME coupling.[87]

The similar change observed in the magnetic properties with the application of – 3 kV/cm and +3 kV/cm indicate the existence of biquadratic (P^2M^2) coupling, where P- ferroelectric polarization and M- magnetization. If the interaction term is really P^2M^2, then the application of +E is the same as -E, and M cannot switch; similarly, the application of +H is the same as -H, and P cannot switch.[10, 88]

In Co-doped BTO ceramics, the paraelectric cubic to ferroelectric tetragonal phase transition is observed at T_C ~110 ºC and the value of T_C is found to be lowered with Co doping. Staruch *et al*.[89] reported the magneto-electric coupling with a weak ferromagnetism in 0.5%Fe-doped BTO single crystals. The temperature dependent capacitance and loss tangent of 0.5%Fe-doped BTO single crystals exhibit cubic to tetragonal, tetragonal to orthorhombic, and orthorhombic to rhombohedral phase transitions. Around ~ 20 K they reported the crystal structure to be rhombohedral. Therefore, while not explicitly measured, we expect that the 7.5%Co-doped BTO ceramic belongs to the rhombohedral phase at ~20 K where the magneto-electric property has been investigated.

Conclusions:

We have synthesized a Pb-free, $BaTi_{1-x}Co_xO_3$ (BTCO) with x = 0.035, 0.05 and 0.075 single phase magnetoelectric material with a tetragonal crystal structure with *P4mm* space group. We observed the decrease of tetragonality ratio with increasing cobalt content. A Fano-like asymmetric peak ~ 173 cm^{-1} [$A_1(LO_1)$] is observed in all the cobalt doped BTO samples. All the samples exhibit a ferroelectric transition temperature above room temperature, which shifts to lower temperatures with increasing cobalt content. All the samples show well saturated ferroelectric hysteretic behavior with large polarization, low leakage current and low dielectric loss tangent at room temperature. The BTCO3 sample exhibits paramagnetic behavior whereas BTCO5 and BTO7 samples show ferromagnetic ordering below 43 K. Magnetic measurements below the ferromagnetic transition temperature with an *in situ* electric field applied reveal significant ME coupling indicating a strong coupling between ferroelectric and magnetic order parameters.

Acknowledgments:

DKP acknowledges support from the U. S. Department of Energy (DOE) under Grant No. DE-SC0002136. PDR acknowledges the Center for Nanophase Materials Sciences, which is a DOE Office of Science User Facility. DAG and NT acknowledge the support by the U.S. Department of Energy, Office of Science, Office of Basic Research CAREER program under Award Number DE-SC0021344.

Data Availability Statement:

The data that supports the findings of this study are available within the article [and its supplementary material].

Competing Interests:

The authors declare no competing financial and/or non-financial interest.

Contributions:

The ideas for the work came from DKP and PDR. The synthesis of samples and XRD, dielectric, SEM, Raman, XPS measurements were carried out by HSM, KB, SK, MMR, DKP and DKP. Raman and XPS measurements were performed by SK and MMR. Ferroelectric, I-V and PUND measurements were carried out by RK and AK. Magnetic and ME coupling measurements were carried out by NT and DAG. All authors cowrote and commented on the manuscript and approved for submission. PDR supervised this work.

Figure Captions:

Fig. 1. (Color online) (a) Rietveld refined XRD patterns of BTCO3, BTCO5 and BTCO7 ceramics using Fullprof Suite software (b) Crystal structure of BTCO.

Fig. 2. (Color online) **(**a) The Fitted Raman scattering spectra of BTCO3, BTCO5 and BTCO7. The spectra were fitted by the Eq. (2). (b) CP behavior of BTCO3, BTCO5 and BTCO7 (c) The FWHM of the CP (upper part) and frequency and FWHM of the $E(TO_1)$ mode as a function of cobalt concentration.

Fig. 3. (Color online) XPS spectra of (a,b) Ba and Co and (c) O at room temperature of BTCO7 sample.

Fig. 4. (Color online) Scanning electron micrographs and EDS maps of (a) large area of 30 × 20 μm (b) on a single grain of BTCO7 ceramics.

Fig. 5. (Color online) (a, c, e) Temperature dependent dielectric permittivity (left panel) and dielectric loss (right panel) and (b, d, f) modified Curie-Weiss law fit of BTCO3, BTCO5 and BTCO7 samples, respectively.

Fig. 6. (Color online) Nyquist plot of (a) BTCO3 (b) BTCO5 (c) BTCO7 samples at different temperature, inset shows the calculations of the activation energy from the Arrhenius equation.

Fig. 7. (Color online) Frequency dependent ac conductivity of (a) BTCO3 (b) BTCO5 (c) BTCO7 samples at different temperature, inset shows the calculations of the activation energy from the Arrhenius equation.

Fig. 8. (Color online) (a) Electric field dependent polarization hysteresis loops of unpoled and poled samples of BTCO3, BTCO5 and BTCO7 samples at RT (b) time profile of applied electric field (upper panel), positive up negative down measurement (lower panel) at RT of BTCO5 sample (c) current density (J) as function of electric field (E) of BTCO3, BTCO5 and BTCO7 samples at RT (inset: J-E curve of unpoled and poled BTCO3 sample).

Fig. 9. (Color online) (a, c) Temperature and (b, d) magnetic field dependent magnetization of BTCO3 and BTCO5 samples, respectively.

Fig. 10. (Color online) (a) Temperature dependent magnetization, magnetic field dependent magnetization (b) at 2K (c) 4-40 K (d) 50-400 K for the BTCO7 sample.

Fig. 11. (Color online) Magnetic hysteresis loops of BTCO7 sample measured at 20 K, in the unpoled state (black), and subsequent *in situ* electric fields of +3 kV/cm (red) and -3 kV/cm (blue).

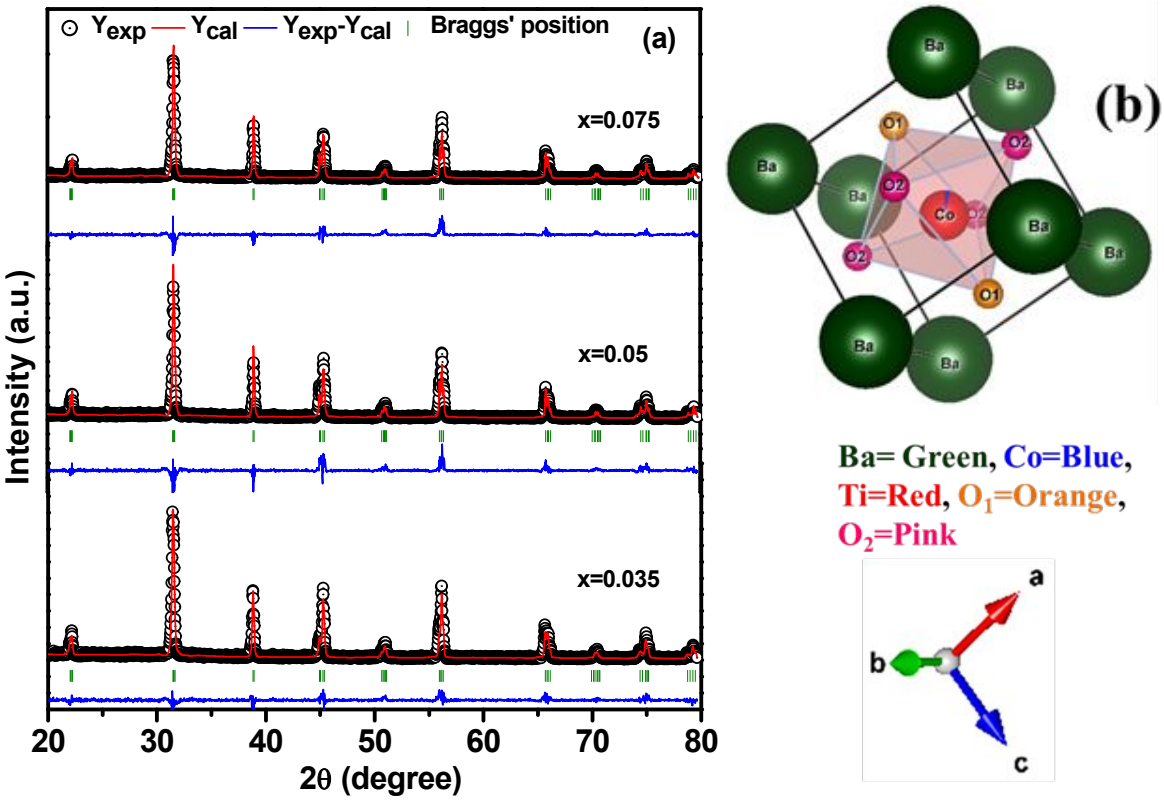

Fig. 1. Pradhan et. al.

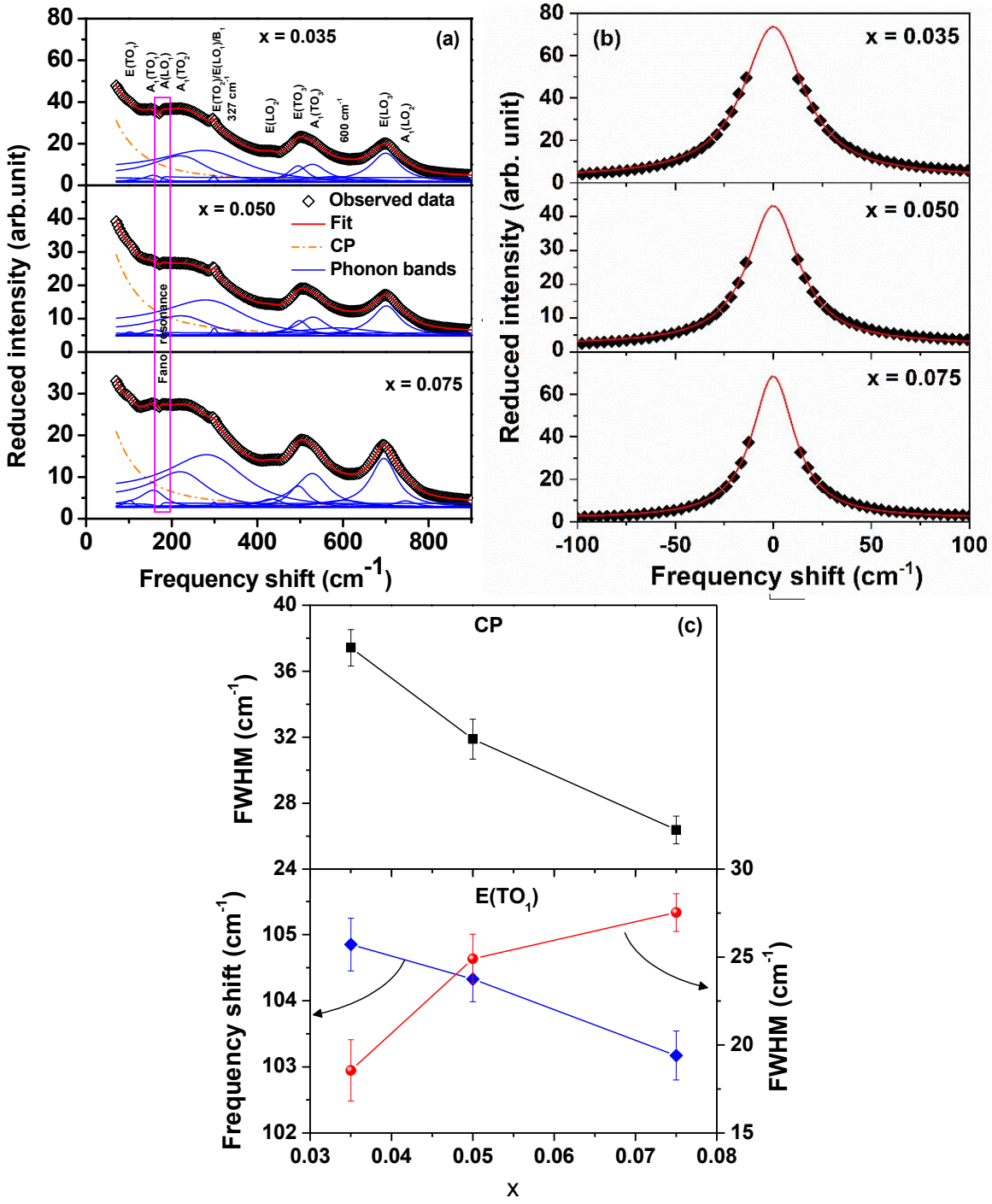
(a)
x = 0.035
x = 0.050
x = 0.075
Observed data
Fit
CP
Phonon bands
Fano resonance
E(TO1)
A1(TO1)
A1(LO1)
A1(TO2)
E(TO2)/E(LO1)/B1, 327 cm-1
E(LO2)
E(TO3)
A1(TO3)
600 cm-1
E(LO3)
A1(LO2)
Reduced intensity (arb.unit)
Frequency shift (cm-1)
(b)
x = 0.035
x = 0.050
x = 0.075
Reduced intensity (arb. unit)
Frequency shift (cm-1)
(c)
CP
FWHM (cm-1)
E(TO1)
Frequency shift (cm-1)
FWHM (cm-1)
x

Fig. 2. Pradhan et. al.

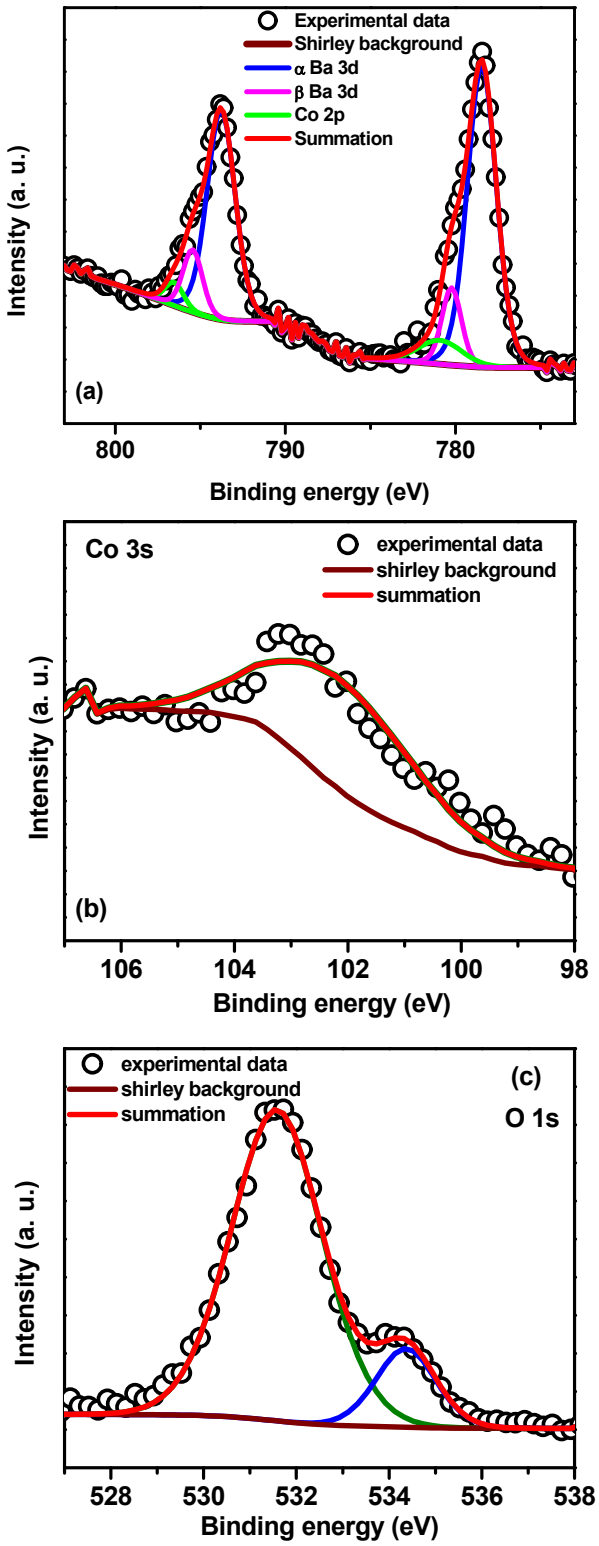

Fig. 3. Pradhan et. al.

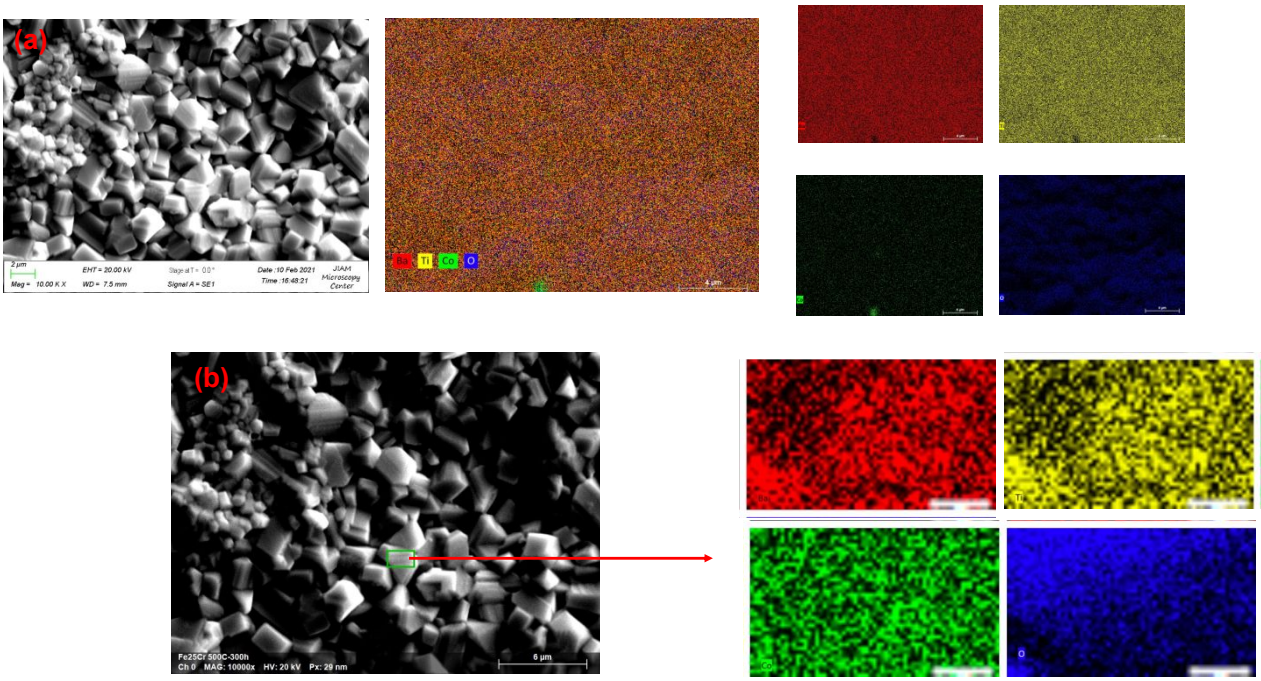

Fig. 4. Pradhan et. al.

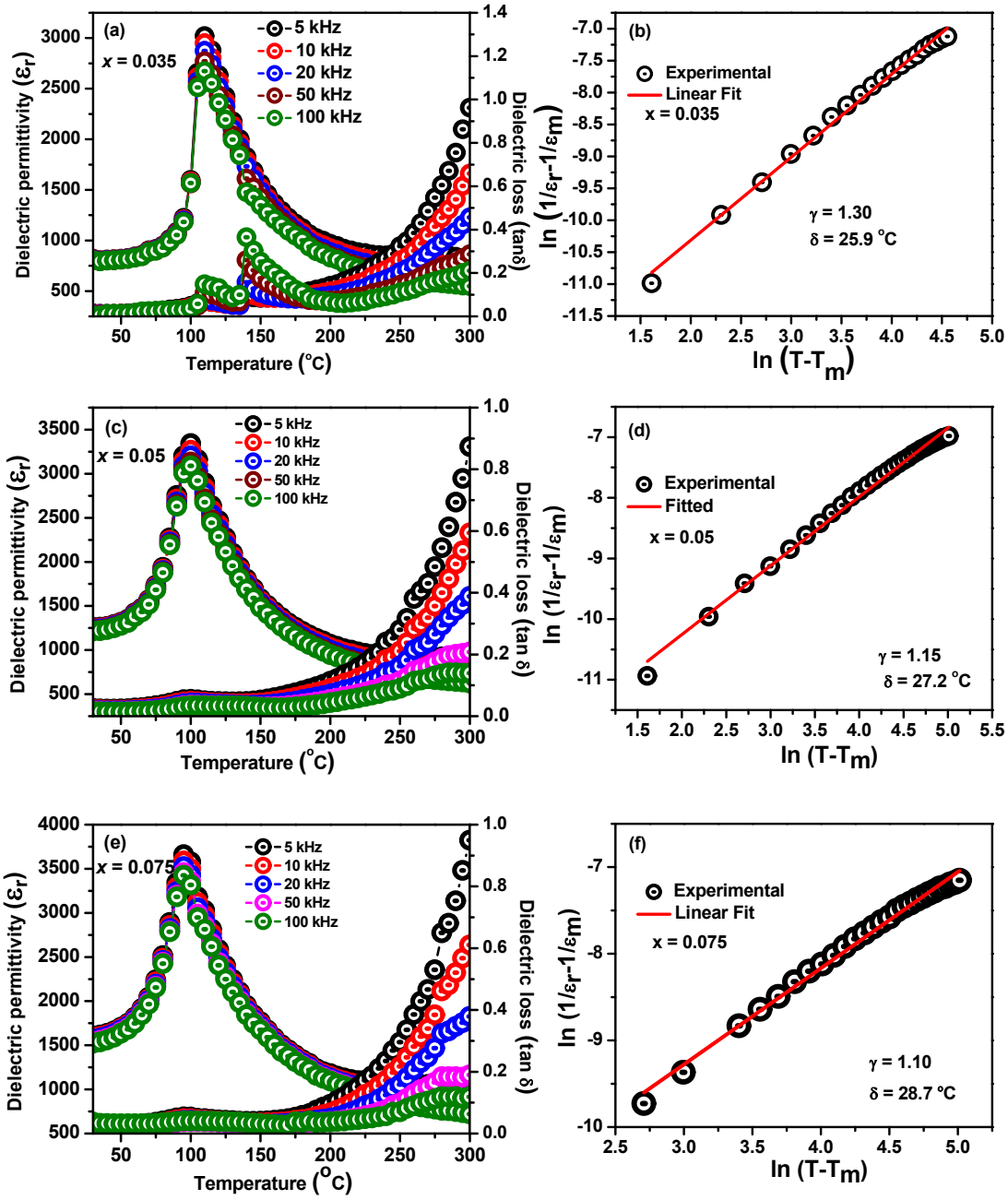

Fig. 5. Pradhan et. al.

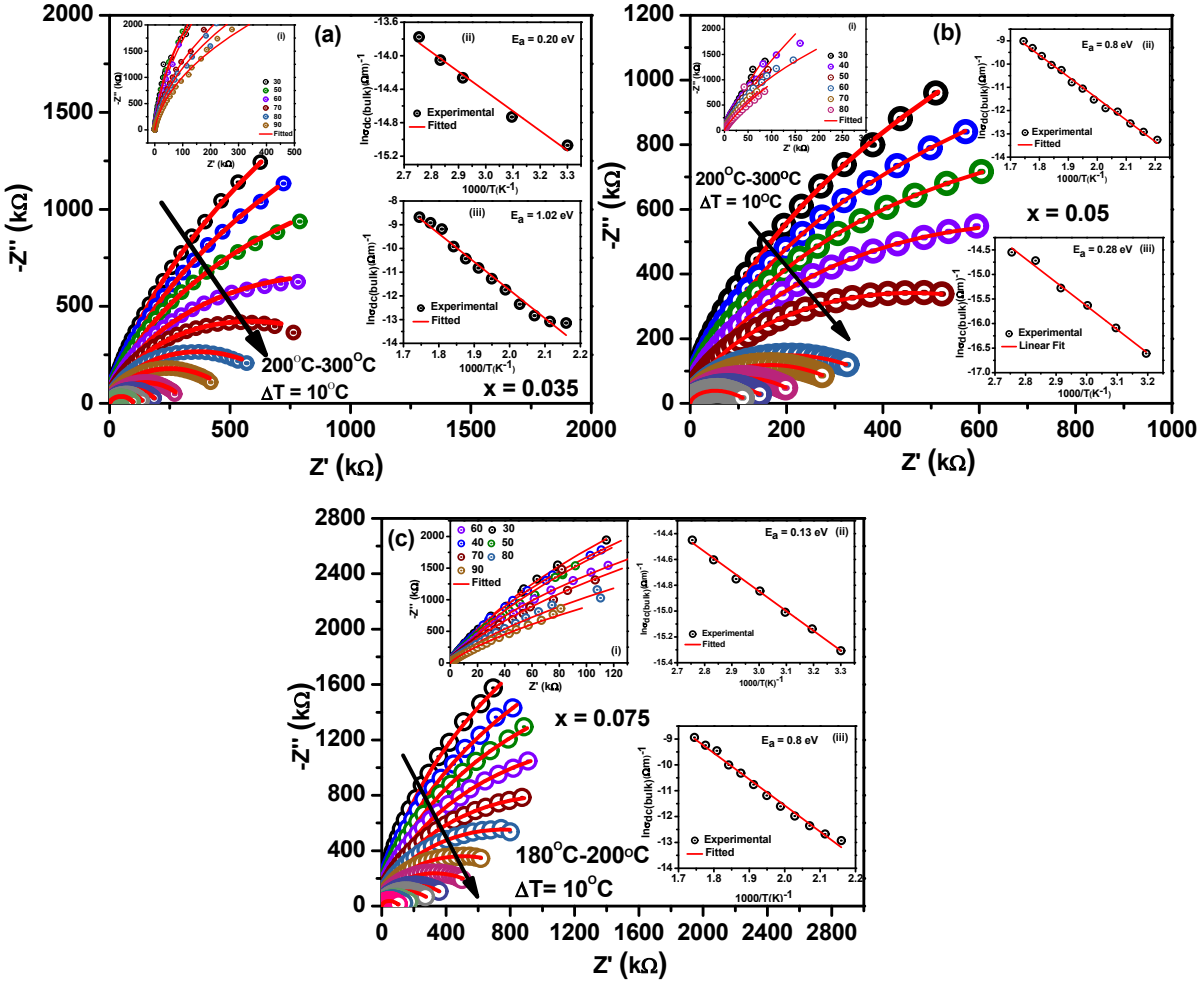

Fig. 6. Pradhan et. al.

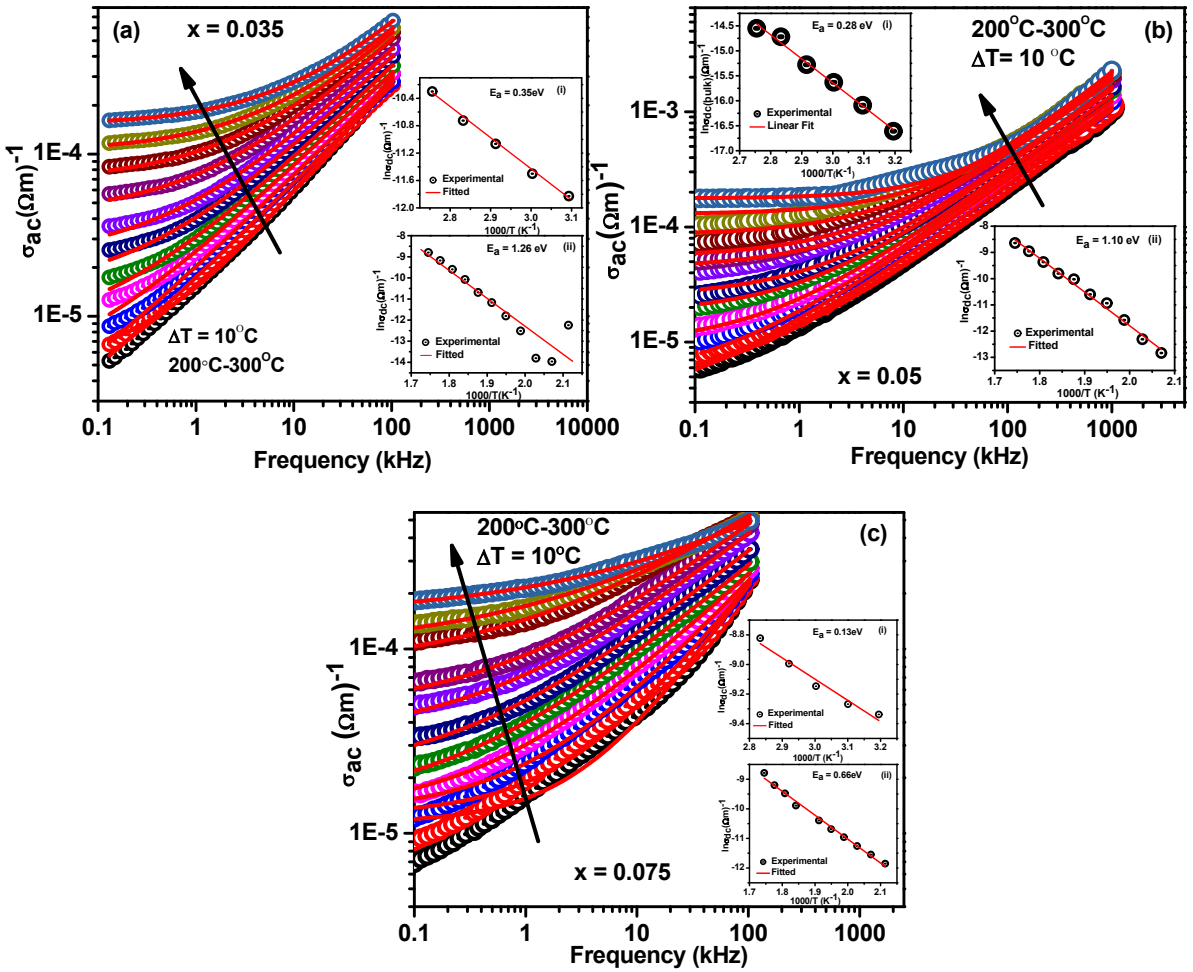

Fig. 7. Pradhan et. al.

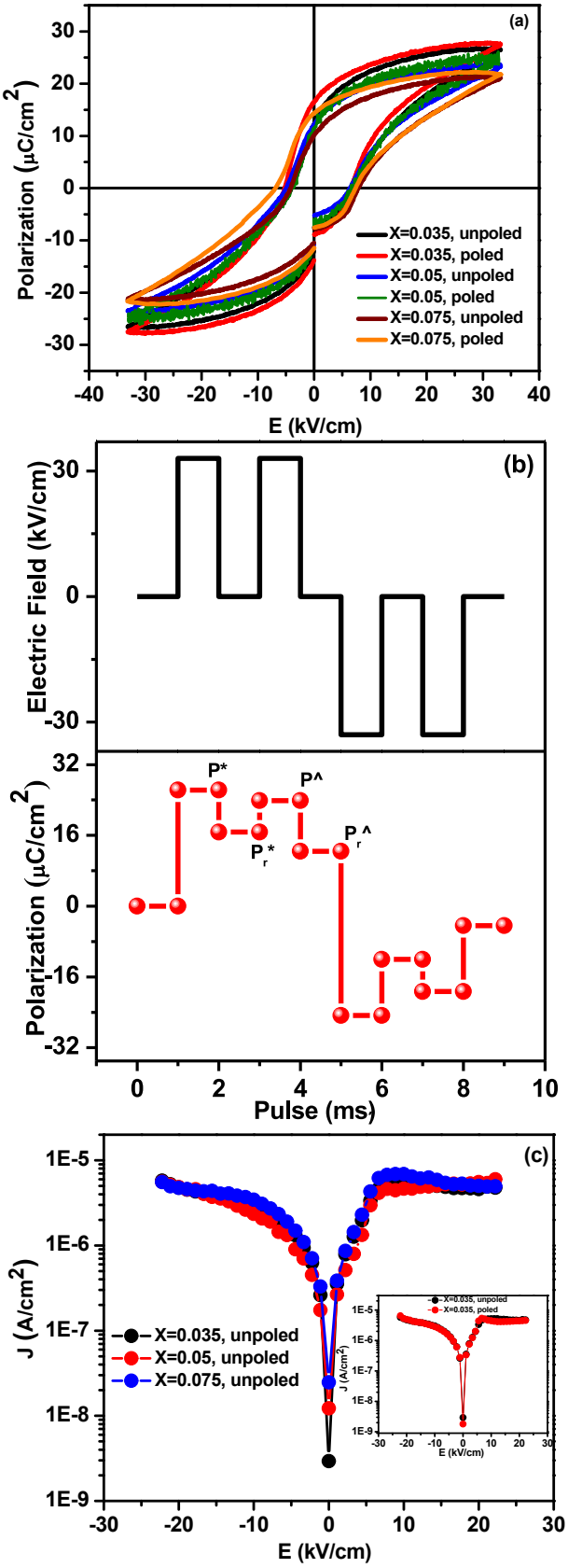

Fig. 8. Pradhan et. al.

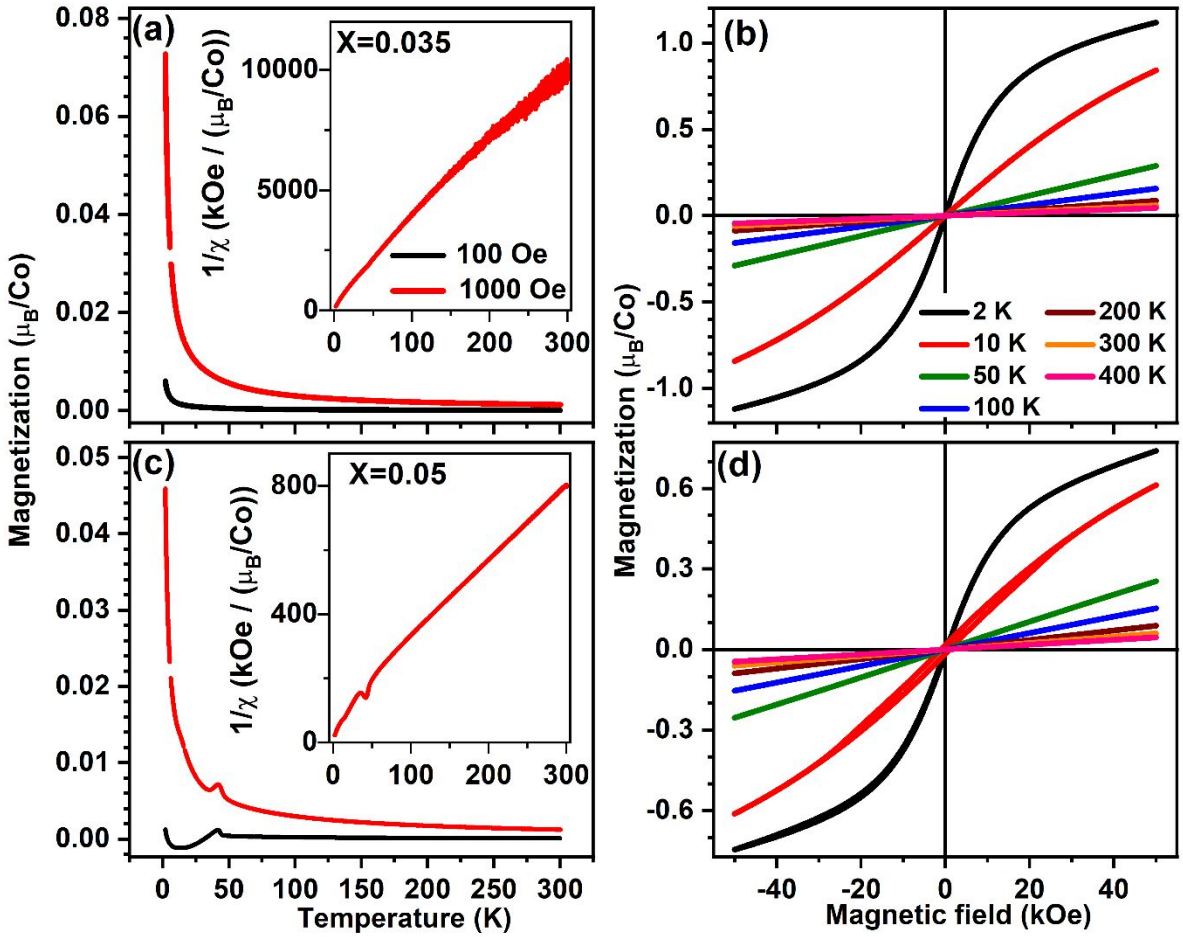

Fig. 9. Pradhan et. al.

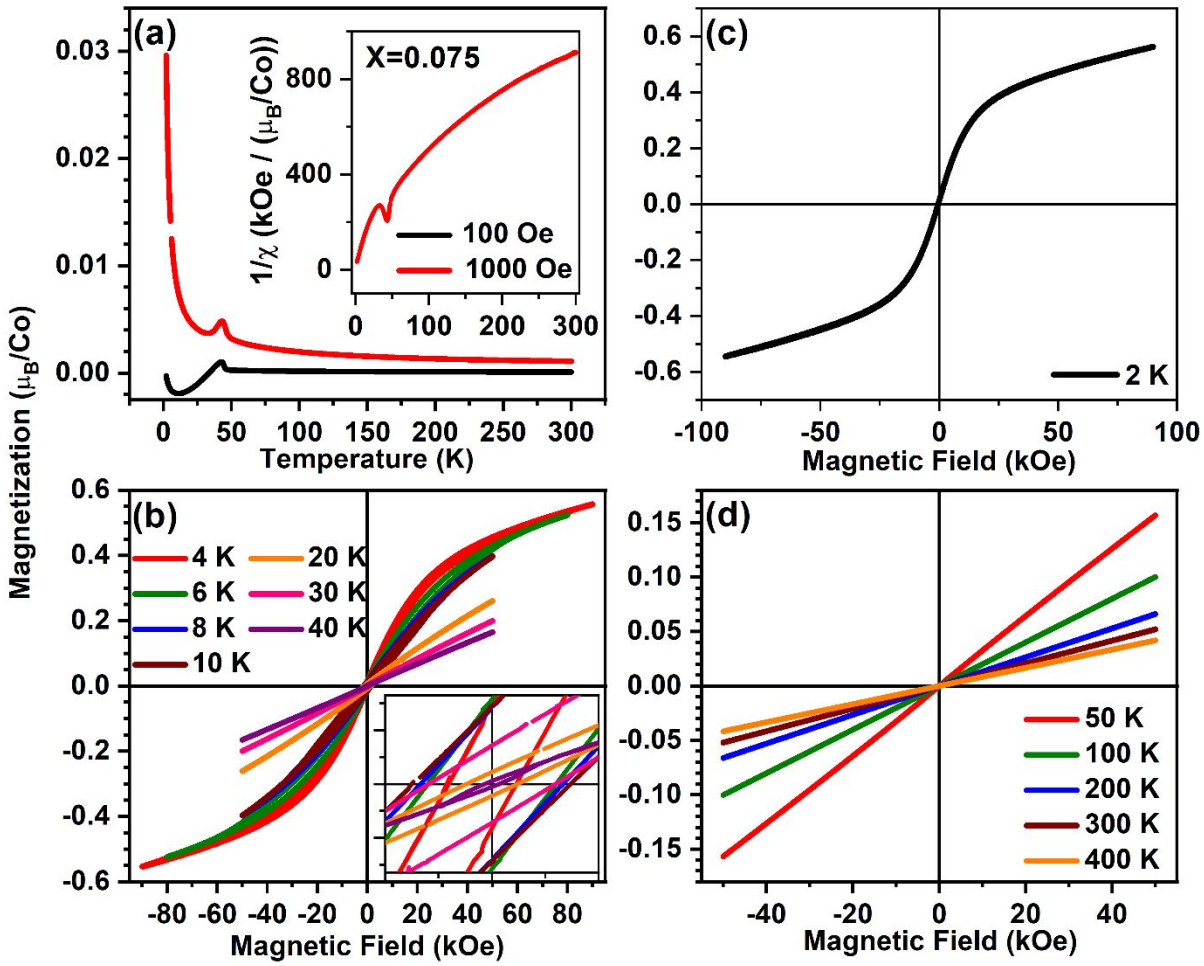

Fig. 10. Pradhan et. al.

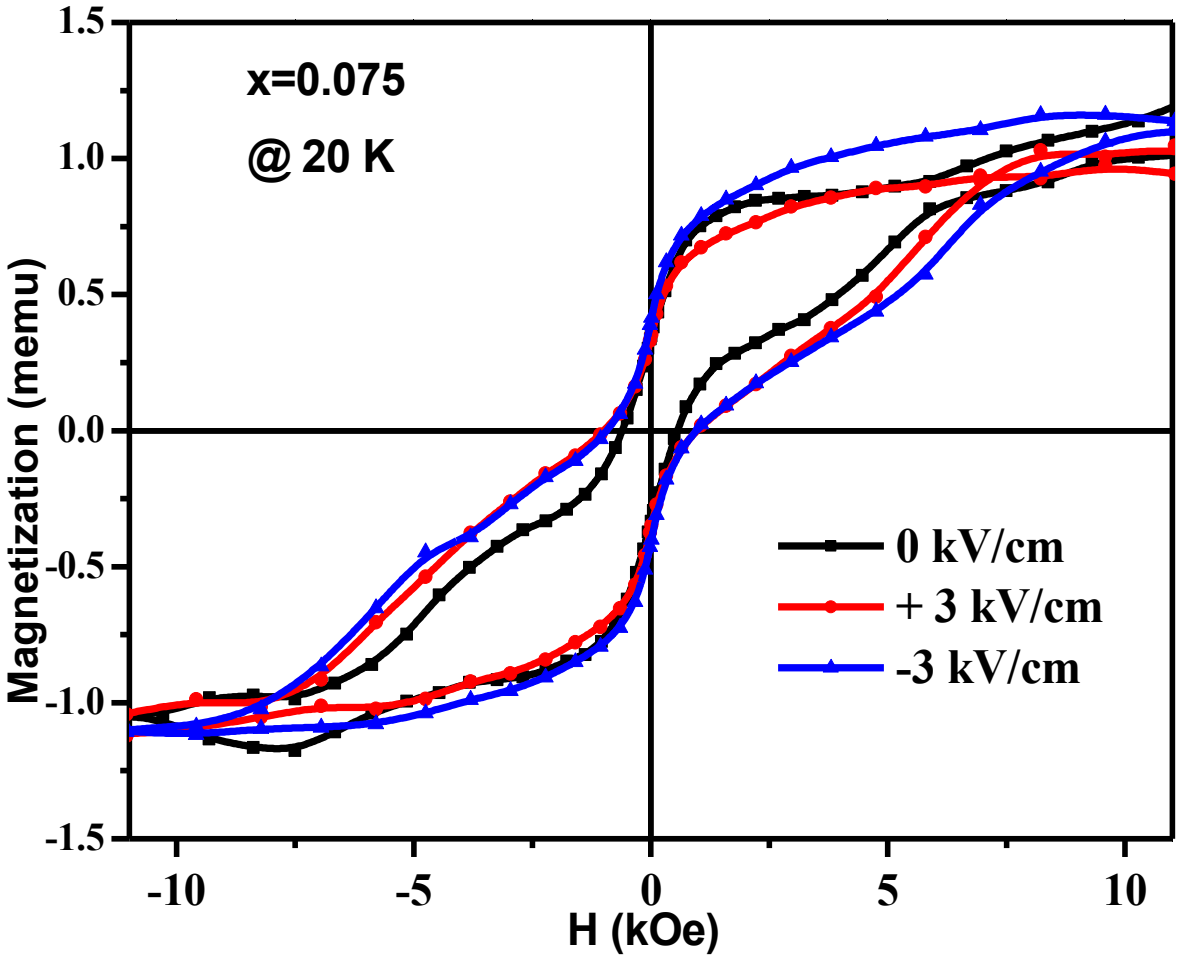

Fig. 11. Pradhan et. al.

References:

1. M. Fiebig, *Journal of physics D: applied physics*, 2005, **38**, R123.
2. W. Eerenstein, N. Mathur and J. F. Scott, *nature*, 2006, **442**, 759-765.
3. N. A. Spaldin and R. Ramesh, *Nature materials*, 2019, **18**, 203.
4. D. K. Pradhan, S. Kumari and P. D. Rack, *Nanomaterials*, 2020, **10**, 2072.
5. S. Manipatruni, D. E. Nikonov, C.-C. Lin, T. A. Gosavi, H. Liu, B. Prasad, Y.-L. Huang, E. Bonturim, R. Ramesh and I. A. Young, *Nature*, 2019, **565**, 35-42.
6. N. A. Hill, *Journal*, 2000.
7. M. Fiebig, T. Lottermoser, D. Meier and M. Trassin, *Nature Reviews Materials*, 2016, **1**, 16046.
8. J. Ma, J. Hu, Z. Li and C. W. Nan, *Advanced materials*, 2011, **23**, 1062-1087.
9. D. K. Pradhan, V. S. Puli, S. Narayan Tripathy, D. K. Pradhan, J. Scott and R. S. Katiyar, *Journal of Applied Physics*, 2013, **114**, 234106.
10. D. M. Evans, M. Alexe, A. Schilling, A. Kumar, D. Sanchez, N. Ortega, R. S. Katiyar, J. F. Scott and J. M. Gregg, *Advanced Materials*, 2015, **27**, 6068-6073.
11. D. K. Pradhan, S. Kumari, R. K. Vasudevan, S. Dugu, P. T. Das, V. S. Puli, D. K. Pradhan, S. V. Kalinin, R. S. Katiyar and P. D. Rack, *Journal of Applied Physics*, 2020, **127**, 194104.
12. D. K. Pradhan, S. Kumari, V. S. Puli, D. K. Pradhan, A. Kumar, S. V. Kalinin, R. K. Vasudevan, R. S. Katiyar and P. D. Rack, *Journal of Materials Chemistry C*, 2020.
13. D. K. Pradhan, S. Kumari, R. K. Vasudevan, E. Strelcov, V. S. Puli, D. K. Pradhan, A. Kumar, J. M. Gregg, A. Pradhan and S. V. Kalinin, *SCIENtIfIC REPoRts*, 2018, **8**, 1-11.
14. C.-W. Nan, M. Bichurin, S. Dong, D. Viehland and G. Srinivasan, *Journal of applied physics*, 2008, **103**, 1.
15. S. Kumari, D. K. Pradhan, N. Ortega, K. Pradhan, C. DeVreugd, G. Srinivasan, A. Kumar, T. R. Paudel, E. Y. Tsymbal and A. M. Bumstead, *Physical Review B*, 2017, **95**, 214109.
16. E. Gradauskaite, J. Gardner, R. M. Smith, F. D. Morrison, S. L. Lee, R. S. Katiyar and J. F. Scott, *Physical Review B*, 2017, **96**, 104104.
17. Z. Ren, G. Xu, X. Wei, Y. Liu, X. Hou, P. Du, W. Weng, G. Shen and G. Han, *Applied Physics Letters*, 2007, **91**, 063106.
18. W. Zhou, H. Deng, L. Yu, P. Yang and J. Chu, *Journal of Applied Physics*, 2015, **117**, 194102.
19. W. Bai, X. Meng, T. Lin, L. Tian, C. Jing, W. Liu, J. Ma, J. Sun and J. Chu, *Journal of Applied Physics*, 2009, **106**, 124908.
20. L. Dong, D. S. Stone and R. S. Lakes, *Journal of Applied Physics*, 2012, **111**, 084107.
21. S. Shao, J. Zhang, Z. Zhang, P. Zheng, M. Zhao, J. Li and C. Wang, *Journal of Physics D: Applied Physics*, 2008, **41**, 125408.
22. Z. Zhao, V. Buscaglia, M. Viviani, M. T. Buscaglia, L. Mitoseriu, A. Testino, M. Nygren, M. Johnsson and P. Nanni, *Physical Review B*, 2004, **70**, 024107.
23. K. Kinoshita and A. Yamaji, *Journal of applied physics*, 1976, **47**, 371-373.
24. F. Gu, É. Murray and P. Tangney, *Physical Review Materials*, 2021, **5**, 034414.
25. C. Lian, Z. A. Ali, H. Kwon and B. M. Wong, *The journal of physical chemistry letters*, 2019, **10**, 3402-3407.
26. H. Nakayama and H. Katayama-Yoshida, *Japanese journal of applied physics*, 2001, **40**, L1355.
27. J. Shah and R. K. Kotnala, *Journal of Materials Chemistry A*, 2013, **1**, 8601-8608.
28. D. Cao, B. Liu, H. Yu, W. Hu and M. Cai, *The European Physical Journal B*, 2015, **88**, 1-7.
29. B. Xu, K. Yin, J. Lin, Y. Xia, X. Wan, J. Yin, X. Bai, J. Du and Z. Liu, *Physical Review B*, 2009, **79**, 134109.
30. F. Lin, D. Jiang, X. Ma and W. Shi, *Journal of Magnetism and Magnetic Materials*, 2008, **320**, 691-694.
31. T.-L. Phan, P. Zhang, D. Grinting, S. Yu, N. Nghia, N. Dang and V. Lam, *Journal of Applied Physics*, 2012, **112**, 013909.
32. Y. Shuai, S. Zhou, D. Bürger, H. Reuther, I. Skorupa, V. John, M. Helm and H. Schmidt, *Journal of Applied Physics*, 2011, **109**, 084105.
33. H. Liu, B. Cao and C. O'Connor, *Journal of Applied Physics*, 2011, **109**, 07B516.

34. P. Ponath, A. O'Hara, H.-X. Cao, A. B. Posadas, R. Vasudevan, M. B. Okatan, S. Jesse, M. Berg, Z. Li and D. Zhang, *Physical Review B*, 2016, **94**, 205121.
35. Y.-H. Lin, S. Zhang, C. Deng, Y. Zhang, X. Wang and C.-W. Nan, *Applied Physics Letters*, 2008, **92**, 112501.
36. L. Luo, Y. Zhao, H. Tian, J. Yang, H. Zhang, J. Li, J. Ding, B. He, S. Wei and C. Gao, *Applied Physics Letters*, 2008, **92**, 232507.
37. J. Rodríguez-Carvajal, *Physica B: Condensed Matter*, 1993, **192**, 55-69.
38. T.-L. Phan, P. Thang, T. Ho, T. Manh, T. D. Thanh, V. Lam, N. Dang and S. Yu, *Journal of Applied Physics*, 2015, **117**, 17D904.
39. L. Padilla-Campos, D. E. Diaz-Droguett, R. Lavín and S. Fuentes, *Journal of Molecular Structure*, 2015, **1099**, 502-509.
40. M. Rahaman, T. Imai, T. Sakamoto and S. Kojima, *Integrated Ferroelectrics*, 2017, **185**, 22-30.
41. M. Rahaman, T. Imai, T. Sakamoto, S. Tsukada and S. Kojima, *Scientific reports*, 2016, **6**, 1-10.
42. M. M. Rahaman, T. Imai, T. Sakamoto, M. Al Helal, S. Tsukada and S. Kojima, *Journal of Alloys and Compounds*, 2018, **735**, 1063-1070.
43. U. D. Venkateswaran, V. M. Naik and R. Naik, *Physical Review B*, 1998, **58**, 14256.
44. G. Burns and B. A. Scott, *Solid State Communications*, 1971, **9**, 813-817.
45. M. DiDomenico Jr, S. Wemple, S. Porto and R. Bauman, *Physical Review*, 1968, **174**, 522.
46. A. Scalabrin, A. Chaves, D. Shim and S. Porto, *physica status solidi (b)*, 1977, **79**, 731-742.
47. J. Freire and R. Katiyar, *Physical Review B*, 1988, **37**, 2074.
48. J. Pokorný, U. Pasha, L. Ben, O. Thakur, D. Sinclair and I. Reaney, *Journal of Applied Physics*, 2011, **109**, 114110.
49. K. Laabidi, M. Fontana and B. Jannot, *Solid state communications*, 1990, **76**, 765-768.
50. N. Dang, T. Thanh, L. Hong, V. Lam and T.-L. Phan, *Journal of Applied Physics*, 2011, **110**, 043914.
51. U. Fano, *Physical Review*, 1961, **124**, 1866.
52. D. Rousseau and S. Porto, *Physical Review Letters*, 1968, **20**, 1354.
53. A. Pinczuk, E. Burstein and S. Ushioda, *Solid State Communications*, 1969, **7**, 139-142.
54. S. Banerjee, D.-I. Kim, R. D. Robinson, I. P. Herman, Y. Mao and S. S. Wong, *Applied physics letters*, 2006, **89**, 223130.
55. J.-H. Ko, T. H. Kim, K. Roleder, D. Rytz and S. Kojima, *Physical Review B*, 2011, **84**, 094123.
56. W. Cochran, *Advances in Physics*, 1960, **9**, 387-423.
57. A. Bussmann-Holder, H. Beige and G. Völkel, *Physical Review B*, 2009, **79**, 184111.
58. M. Fontana, A. Ridah, G. Kugel and C. Carabatos-Nedelec, *Journal of Physics C: Solid State Physics*, 1988, **21**, 5853.
59. G. Burns and B. A. Scott, *Physical Review B*, 1973, **7**, 3088.
60. M. Rahaman, T. Imai, J. Miyazu, J. Kobayashi, S. Tsukada, M. Helal and S. Kojima, *Journal of Applied Physics*, 2014, **116**, 074110.
61. J. Toulouse, F. Jiang, O. Svitelskiy, W. Chen and Z.-G. Ye, *Physical Review B*, 2005, **72**, 184106.
62. J. Baniecki, M. Ishii, T. Shioga, K. Kurihara and S. Miyahara, *Applied physics letters*, 2006, **89**, 162908.
63. V. Craciun and R. Singh, *Applied Physics Letters*, 2000, **76**, 1932-1934.
64. S. C. Petitto, E. M. Marsh, G. A. Carson and M. A. Langell, *Journal of Molecular Catalysis A: Chemical*, 2008, **281**, 49-58.
65. K. A. Bogle, M. N. Bachhav, M. S. Deo, N. Valanoor and S. B. Ogale, *Applied Physics Letters*, 2009, **95**, 203502.
66. L. Bai, M. Sun, W. Ma, J. Yang, J. Zhang and Y. Liu, *Nanomaterials*, 2020, **10**, 1798.
67. J. F. Watts and J. Wolstenholme, 2003.
68. C. Wagner, W. Riggs, L. Davis, J. Moulder and G. Muilenberg, *Eden Prairie, MN*, 1979, 38.
69. S. Balčiūnas, M. Ivanov, J. Banys and S. Wada, *Ferroelectrics*, 2017, **512**, 8-13.
70. C. Ang, Z. Yu and L. Cross, *Physical Review B*, 2000, **62**, 228.
71. R. D. Shannon, *Acta crystallographica section A: crystal physics, diffraction, theoretical and general crystallography*, 1976, **32**, 751-767.

72. I. Levin, M. C. Stennett, G. C. Miles, D. I. Woodward, A. R. West and I. M. Reaney, *Applied physics letters*, 2006, **89**, 122908.
73. C. Fang, L. Chen and D. Zhou, *Physica B: Condensed Matter*, 2013, **409**, 83-86.
74. S. Dash, H. S. Mohanty, K. Bhoi, R. Kant, A. Kumar, R. Thomas and D. K. Pradhan, *Journal of Materials Science: Materials in Electronics*, 2018, **29**, 20820-20831.
75. D. K. Pradhan, S. Kumari, V. S. Puli, D. K. Pradhan, A. Kumar, S. V. Kalinin, R. K. Vasudevan, R. S. Katiyar and P. D. Rack, *Journal of Materials Chemistry C*, 2020, **8**, 12113-12122.
76. D. Viehland, S. Jang, L. E. Cross and M. Wuttig, *Physical Review B*, 1992, **46**, 8003.
77. D. K. Pradhan, R. Choudhary, C. Rinaldi and R. Katiyar, *Journal of Applied Physics*, 2009, **106**, 024102.
78. H. S. Mohanty, A. Kumar, B. Sahoo, P. K. Kurliya and D. K. Pradhan, *Journal of Materials Science: Materials in Electronics*, 2018, **29**, 6966-6977.
79. N. Maso, H. Beltran, E. Cordoncillo, P. Escribano and A. West, *Journal of Materials Chemistry*, 2006, **16**, 1626-1633.
80. O. Raymond, R. Font, J. Portelles, N. Suárez-Almodovar and J. Siqueiros, *Journal of applied physics*, 2006, **99**, 124101.
81. C. Wang, C. Lei, G. Wang, X. Sun, T. Li, S. Huang, H. Wang and Y. Li, *Journal of Applied Physics*, 2013, **113**, 094103.
82. G. Singh, V. Tiwari and P. Gupta, *Journal of Applied Physics*, 2010, **107**, 064103.
83. O. Bidault, M. Maglione, M. Actis, M. Kchikech and B. Salce, *Physical Review B*, 1995, **52**, 4191.
84. J. Yang, J. Kim, J. Lee, S. Woo, J. Kwak, J. Hong and M. Jung, *Physical Review B*, 2008, **78**, 094415.
85. S. Kumari, N. Mottaghi, C.-Y. Huang, R. Trappen, G. Bhandari, S. Yousefi, G. Cabrera, M. S. Seehra and M. B. Holcomb, *Scientific Reports*, 2020, **10**, 1-11.
86. N. Mottaghi, R. B. Trappen, S. Kumari, C. Huang, S. Yousefi, G. B. Cabrera, M. Aziziha, A. Haertter, M. B. Johnson and M. S. Seehra, *Journal of Physics: Condensed Matter*, 2018, **30**, 405804.
87. D. K. Pradhan, S. Sahoo, S. K. Barik, V. S. Puli, P. Misra and R. S. Katiyar, *Journal of Applied Physics*, 2014, **115**, 194105.
88. M. Daraktchiev, G. Catalan and J. F. Scott, *Physical Review B*, 2010, **81**, 224118.
89. M. Staruch, H. ElBidweihy, M. Cain, P. Thompson, C. Lucas and P. Finkel, *APL Materials*, 2020, **8**, 031109.